

The high-resolution version of TM5-MP for optimised satellite retrievals: Description and Validation.

J. E. Williams¹, K. F. Boersma^{1,2}, P. Le Sager¹, W. W. Verstraeten^{1,2,3}

[1] {KNMI, De Bilt, The Netherlands}

[2] {Meteorology and Air Quality Group, Wageningen University, Wageningen, The Netherlands}

[3] {KMI, Ukkel, Brussels, Belgium}

Abstract

We provide a comprehensive description of the high-resolution version of the TM5-MP global Chemistry-Transport Model, which is to be employed for deriving highly resolved vertical profiles of nitrogen dioxide (NO₂), formaldehyde (CH₂O), and sulphur dioxide (SO₂) for use in satellite retrievals from platforms such as the Ozone Monitoring Instrument (OMI) and the Sentinel-5 Precursor, the TROPOspheric Monitoring Instrument (tropOMI). Comparing simulations conducted at horizontal resolutions of 3° x 2° and 1° x 1° reveals differences of ±20% exist in the global seasonal distribution of ²²²Rn, being larger near specific coastal locations and tropical oceans. For tropospheric ozone (O₃), analysis of the chemical budget terms shows that the impact on globally integrated photolysis rates is rather low, in spite of the higher spatial variability of meteorological data fields from ERA-Interim at 1° x 1°. Surface concentrations of O₃ in high-NO_x regions decrease between 5-10% at 1° x 1° due to a reduction in NO_x recycling terms and an increase in the associated titration term of O₃ by NO. At 1° x 1°, the net global stratosphere-troposphere exchange of O₃ decreases by ~7%, with an associated shift in the hemispheric gradient. By comparing NO, NO₂, HNO₃ and PAN profiles against measurement composites, we show that TM5-MP captures the vertical distribution of NO_x and long-lived NO_x reservoirs at background locations, again with modest changes at 1° x 1°. Comparing monthly mean distributions in lightning NO_x and applying ERA-interim convective mass fluxes, we show that the vertical redistribution of lightning NO_x changes with enhanced release of NO_x in the upper troposphere. We show that surface mixing ratios in both NO and NO₂ are generally underestimated in both low and high NO_x scenarios. For Europe, a negative bias exists for [NO] at the surface across the whole domain, with lower biases at 1° x 1° at only ~20% of sites. For NO₂, biases are more variable, with lower (higher) biases at 1° x 1° occurring at ~35% (~20%) of sites, with the remainder showing little change. For CH₂O, the impact of higher resolution on the chemical budget terms is rather modest, with changes less than 5%. The simulated vertical distribution of CH₂O agrees reasonably well with measurements in pristine locations, although column-integrated values are generally underestimated relative to satellite measurements in polluted regions. For SO₂, the performance at 1° x 1° is principally governed by the quality of the emission inventory, with limited improvements in the site specific biases with most showing no significant improvement. For the vertical column, improvements near strong source regions occur which reduce the biases in the integrated column. For remote regions missing biogenic source terms are inferred.

1. Introduction

One application of Chemistry Transport Models (CTM) is to provide accurate vertical and horizontal global distributions of trace gases such as ozone (O_3), nitrogen dioxide (NO_2), sulphur dioxide (SO_2) and formaldehyde (CH_2O) that are used as *a-priori* best-guesses in the retrievals of tropospheric abundances from instruments mounted on Earth-orbiting satellites such as the Tropospheric Emission Sounder (TES; Worden et al., 2007) Global Ozone Monitoring Experiment (GOME), SCanning Imaging Absorption spectroMeter for Atmospheric CHartographY (SCIAMACHY; De Smedt et al., 2008), the Ozone Monitoring Instrument (OMI; Boersma et al., 2011), and GOME-2 (Valks et al., 2011). To date, although high-resolution regional models have been employed for selected regions such as the US and Europe (e.g. Russell et al., 2011; Zhou et al., 2012; Vinken et al., 2014), at the global scale the CTMs resolutions employed are still rather coarse (between $1.1-4.0^\circ$ latitude and $1.1-6^\circ$ longitude), resulting in ‘footprints’ which aggregate hundreds of kilometers in area. This has limitations as the resulting total columns are sensitive to topography, surface albedo and the shape of the *a-priori* vertical profiles themselves. Using rather coarse resolution leads to substantial errors in the retrievals (e.g. Boersma et al., 2007; Heckel et al., 2011; Russell et al., 2011) and imposes limitations towards capturing the regional scale variability in short-lived trace gas abundances observed from high-resolution satellite instruments such as OMI.

This lack of spatial detail is particularly relevant for situations where strong spatio-temporal variability in the vertical distribution of NO_2 , SO_2 , and CH_2O can be expected. Examples include shipping lanes in the relatively unpolluted marine boundary layer (e.g. Vinken et al., 2014) and coal-fired power plant SO_2 pollution (e.g. Fioletov et al., 2015). Moreover, during the day the local lifetime and mixing ratios of trace gases such as nitric oxide (NO) and NO_2 are critically dependent on a host of variables e.g. temperature, surface albedo, cloud cover (via photolysis), chemical conversion (i.e. NO/ NO_2 ratio) and the extent of mixing by convective upwelling (i.e. land type) and advective transport. Thus, the information provided for the retrievals is affected by the coarsening of the high-resolution meteorological data used to drive the CTM. Recently, Heckel et al. (2011) demonstrated that there is an associated uncertainty of ~ 2 using *a-priori* data from a global CTM rather than a regional CTM, principally due to loss of spatial information. Two other studies focusing on the impact of horizontal resolution on the retrieval of vertical column densities of NO_2 suggested that errors of up to $\sim 50\%$ exist (Yamaji et al., 2014; Lin et al., 2014). This problem becomes accentuated for the next generation of Earth-orbiting satellites such as the Tropospheric Monitoring Instrument (tropOMI), which has a smaller footprint compared to its predecessors (Veeffkind et al., 2012). Applications of TM5 include the retrieval of NO_2 , CH_2O , and SO_2 column densities from OMI and tropOMI (e.g. van Geffen et al., 2016), where studies related to the influence of horizontal resolution have been limited principally to NO_2 .

The dominant tropospheric loss terms for CH_2O are photolysis and scavenging into cloud droplets (wet deposition; Jacob, 2000). Thus the atmospheric lifetime of CH_2O is highly sensitive to the extent of cloud cover and the vertical profiles of the photolysis rates. A dominant application of CH_2O retrievals is to provide constraints on tropical and sub-tropical isoprene emission fluxes (e.g. Palmer et al., 2006; Stavrou et al., 2009; Marais et al., 2012). The resulting emission estimates are highly sensitive to the stoichiometric yield of CH_2O from isoprene oxidation, the chemical lifetime of CH_2O and spatial differences in land cover. Other applications include estimating emissions released during Biomass Burning (BB) episodes (Gonzi et al., 2011),

whose spatial location is also smeared via coarsening in TM5-MP. For SO_2 , which predominantly originates from point sources, an adequate spatial distribution of such sources is crucial for estimating accurate biases in existing emission inventories.

In this paper we provide a comprehensive description of the global, high-resolution $1^\circ \times 1^\circ$ version of the TM5 CTM tailored for the application of satellite retrievals (hereafter referred to as TM5-MP). In Sect. 2 we give details related to the modifications which have been made to the TM5 model compared to previous versions, the emission inventories employed, updates that have been made to the modified CB05 chemical mechanism, the stratospheric boundary conditions, the photolysis scheme, the heterogeneous conversion and the overall model structure. In Sect. 3 we analyse the impact on convective and advective transport of trace species from the BL of both increased horizontal resolution and use of ERA-interim convective mass-fluxes, as derived using radon (^{222}Rn) distributions. In Sect. 4 we investigate the effects on regional and global photolysis frequencies. In Sects. 5-9 we examine the differences in the vertical and horizontal distributions of tropospheric O_3 , NO_x , Lightning induced NO_x , N-containing species (i.e. nitric acid (HNO_3), peroxy-acetyl-nitrate (PAN) and lumped organic nitrates (ORGNTR)), CH_2O and SO_2 , where we make comparisons against both surface and aircraft measurements to validate mixing ratios. Finally, in Sect. 10, we present our conclusions.

2 Description of TM5-MP

Previous versions of TM5 (TM5-chem-v3.0, Huijnen et al., 2010) included a two-way nested zooming option as described by Krol et al. (2005). This option allowed high-resolution simulations to be performed over any pre-defined regional domain, with boundary conditions being determined by the global simulation at coarser resolution. Typically, global simulations at $3^\circ \times 2^\circ$ with zoom regions at $1^\circ \times 1^\circ$ were performed to alleviate the long runtime of a global $1^\circ \times 1^\circ$ run. In the new version of TM5 (hereafter referred to as TM5-MP; the massively parallel version), the usage of the Message Passing Interface (MPI) has been totally rewritten. Zoom regions are no longer available, but data sets are distributed along longitudes and latitudes, instead of model levels and tracers. The advantages of that overhaul towards domain decomposition are a smaller memory requirement and the possibility to use more processors making global $1^\circ \times 1^\circ$ simulations feasible in terms of runtime and affordable in terms of computing resources. A TM5-MP global $3^\circ \times 2^\circ$ ($1^\circ \times 1^\circ$) run is ~ 6 (~ 20) times faster than the previous version of TM5 (Huijnen et al., 2010) for similar resources. The following model description pertains to both $3^\circ \times 2^\circ$ and $1^\circ \times 1^\circ$ simulations discussed in this manuscript.

Here we provide a comprehensive description of the modifications and updates introduced into TM5-MP compared to TM5 v3.0 (Huijnen et al., 2010). The model is driven using the ERA-interim meteorological reanalysis (Dee et al., 2011) and updated every 3 hours, with interpolation of fields for the intermediate time periods. Although TM5-MP can adopt all 60 vertical levels provided by the ECMWF ERA-Interim reanalysis, we employ 34 vertical levels for this study with higher resolution in the troposphere and Upper Troposphere-Lower Stratosphere (UTLS). Convective mass-fluxes and detrainment rates are taken from ERA-interim dataset to describe the updraft velocities from the Boundary Layer (BL) into the free troposphere, which replaces the parameterization of Tiedtke (1989) used in previous versions. The vertical diffusion in the free

troposphere is calculated according to Louis (1979), and in the BL by the approach of Holtslag and Boville (1993). Diurnal variability in the BL height is determined using the parameterization of Voegele and Holtslag (1996). We use the first-order moments scheme with an iterative time-step to prevent too much mass being transported out of any particular grid-cell during the time-step according to the preservation of the Courant-Friedrichs-Lewy (CFL) criterium (Bregman et al., 2003), which is especially relevant when reducing the size of grid-cells as done here.

The gas-phase chemistry in TM5-MP is described by an expanded version of the modified CB05 chemical mechanism (hereafter mCB05; Williams et al., 2013). We have placed emphasis on updating and expanding the fast NO_x chemistry to account for an accurate partitioning of nitrogen for higher NO_x regimes than those occurring at coarser horizontal resolutions. All reaction rate data is now taken from the latest IUPAC recommendations (sited at <http://iupac.pole-ether.fr/>; last access June 2016) using updated formulations for third-body collisions, where the rate data for fast NO_x and CH₂O chemistry is given in Table 1. This includes the recent update to the formation rate of HNO₃ determined by Möllner et al. (2010). The most relevant modifications are: (i) The yield of CH₂O, methanol (CH₃OH) and the hydro-peroxy radical (HO₂) from the self-termination of the methyl-peroxy radical (CH₃O₂) is increased according to Yarwood et al. (2005), (ii) the direct formation of CH₂O from the reaction of CH₃O₂ + HO₂ is added using the temperature dependent branching ratio defined in Atkinson et al. (2004), (iii) the production of HNO₃ during the oxidation of dimethyl sulphide (DMS) by the NO₃ is now included, (iv) explicit organic peroxy radicals have been introduced as products from the oxidation of propene (C₃H₆) and propane (C₃H₈) by OH, which are lost by either the reaction with nitric oxide (NO) or HO₂ allowing the in-situ chemical formation of acetone (CH₃COCH₃) and higher aldehydes (ALD2), respectively, following the stoichiometry given in Emmons et al. (2010), (v) a second product channel for N₂O₅ photolysis is added producing NO, (vi) the formation and photo-dissociation of HONO has been included, (vii) the formation and transport of methyl peroxy nitrate (CH₃O₂NO₂) is also included (Browne et al., 2011), and (viii) modifications to the gas-phase chemistry involving NH₃ have been introduced following the stoichiometry given in Hauglestone et al. (2014). This version of the modified CB05 chemical mechanism is hereafter referred to as mCB05v2.

The calculation of height resolved photolysis rates (*J* values) is performed using a tailored version of the Modified Band Approach (MBA). The implementation and performance of this parameterization in TM5 has been fully described in Williams et al. (2012). For the calculation of the height-resolved actinic fluxes at the seven specific wavelengths used for calculating the *J* values (these being 205.1nm, 287.9nm, 302.0nm, 311.0nm, 326.5nm, 385.0nm and 610.0nm), the 2-stream radiative transfer solver of Zdunkowski et al. (1980) is embedded into TM5-MP. Details regarding the parameterizations used to account for the scattering and absorption introduced by gaseous molecules, aerosols and clouds the reader is referred to Williams et al. (2012). For aerosols, the climatology of Shettle and Fenn (1979) is included. The calculation of the effective radius (*r_{eff}*) of cloud droplets is now performed using the approach of Martin et al. (1994), where different parameter values are used for over the land and ocean using cloud condensation nuclei concentrations of 40 and 900, respectively. Due to potentially erroneous values at low horizontal resolution, we weight the final *r_{eff}* value using the land fraction in each grid-cell. We apply limits between 4-16μm on the resulting *r_{eff}* values. This improves the representation of the scattering component due to cloud droplets used for the calculation of the actinic flux in the lower troposphere (LT; not shown). For the scattering effects from cloud droplets, we

subsequently downsize the physical r_{eff} by $\sim 0.5\text{-}2\mu\text{m}$ to account for the relationship between the optical and physical r_{eff} values.

For aerosols, an aerosol scheme is available for use within TM5-MP (aan den Brugh et al., 2010), but we choose not to use it for the purpose of satellite retrievals due to the extra computational expense needed when performing high resolution simulations that would potentially hinder operational use. We acknowledge that the description of aerosols in this study is rather crude and increasing scattering could have an impact under instances of low cloud coverage. For the application of TM5-MP towards satellite retrieval, it is preferable to use any advancements in computational performance on further increases in the horizontal resolution employed. Therefore it is not currently envisaged that a full description of aerosol processes will be included during operational satellite retrievals.

However, heterogeneous conversion processes still need the description of the total reactive Surface Area Density (SAD) from aerosols. In TM5-MP this is assumed as the cumulative value of contributions from sulphate, nitrate, ammonium and methane sulphononic acid as calculated by the EQUilibrium Simplified Aerosol Model (EQSAM) approach (Metzer et al., 2002), thus the secondary organic aerosol component is not included. The distribution of these aerosol species is calculated online and coupled to the respective gaseous precursors. The density of each aerosol type (1.7 g/cm^3) and r_{eff} (of between $0.18\text{-}0.2\mu\text{m}$) is prescribed as in Huijnen et al. (2014). Swelling at higher relative humidities ($> 70\%$) is crudely accounted for by increasing r_{eff} between $0.25\text{-}0.27\mu\text{m}$. The contributions due to sea-salt, black carbon and organic carbon towards heterogeneous loss are not accounted for. Temperature dependent gas-phase diffusion co-efficients (D_g) are used in the derivation of the pseudo first-order heterogeneous rate constants based on the theory of Schwartz (1986).

For N_2O_5 , the uptake coefficient (γ) is calculated using the parameterization of Evans and Jacob (2005), therefore dependent on both temperature and relative humidity. Once a surface reaction with H_2O occurs two molecules of HNO_3 are formed. No uptake on cirrus particles is included for HNO_3 , which can lead to denitrification of the upper troposphere (Lawrence and Crutzen, 1998; von Kuhlmann and Lawrence, 2006). For HO_2 we adopt a fixed $\gamma_{\text{HO}_2} = 0.06$ across all aerosol types as taken from Abbatt et al. (2012) and for NO_3 we adopt a fixed $\gamma_{\text{NO}_3} = 10^{-3}$ as recommended by Jacob (2000). For HO_2 , heterogeneous conversion forms 0.5 molecules of Hydrogen Peroxide (H_2O_2), whereas for NO_3 it forms one molecule of HNO_3 following Emmons et al. (2010). For the SAD associated with cloud droplets we use the r_{eff} values that are calculated by Martin et al. (1994) thus maintaining consistency between the size of the cloud droplets used for the scattering component in the calculation of J values and heterogeneous loss rates on the clouds. By using the ECMWF cloud fraction for each respective grid-cell, we assume that instantaneous mixing throughout the grid-cell does not occur in order to avoid exaggerated conversion rates on cloud surfaces.

As TM5-MP contains no explicit stratospheric chemistry, we apply constraints above the tropopause to ensure realistic Stratosphere-Troposphere Exchange (STE) of O_3 and for constraining the incoming radiation reaching the troposphere needed for the MBA (Williams et al., 2012). For stratospheric O_3 , we use total column values derived from the assimilation of satellite observations as provided in the improved version of the Multi-Sensor Re-analysis (MSR, van der A., 2010), which is vertically distributed according to the climatology of Fortuin and Kelder (1998). Three distinct zonal bands are used for nudging the stratospheric O_3 fields, these being

30°S-30°N, 30-66°S/N and > 66°S/N, where nudging occurs at pressure levels <45hPa, <95hPa and <120hPa, with relaxation times of 2.5 days, 3 days and 4 days, respectively.

For stratospheric CH₄ we use the monthly 2D climatological fields provided by Grooß and Russell (2005), with the nudging heights and relaxation times being identical to those used for stratospheric O₃. For stratospheric CO and HNO₃ we constrain mixing ratios by using monthly mean ratios of CO/O₃ (Dupuy et al., 2004) and HNO₃/O₃ (Jégou et al., 2008; Urban et al., 2009) based on the latitudinal climatologies derived from ODIN observations using data for 2003/2004 (CO) and 2001-2009 (HNO₃). In order to avoid jumps in the nudging constraints between months, we gradually change between ratios using the total monthly difference/number of days in the month. These ratios are applied using the monthly mean stratospheric O₃ distribution in TM5-MP, which is constrained by the MSR dataset (van der A et al., 2010). For both species, model fields are nudged at 5.5hPa, 10hPa and 28hPa using relaxation times of 5, 10 and 60 days, respectively. Previous versions of TM5 used a HNO₃ climatology from the UARS MLS instrument and applied nudging constraints at 10hPa only (Huijnen et al., 2010).

For our study on the impact of horizontal resolution on the performance of TM5-MP, we present simulations for the year 2006, which has been used for previous benchmarking studies (Huijnen et al., 2010; Williams et al., 2012). We use a one year spin-up from the same initial conditions, where the initial conditions are representative of the state-of-the-atmosphere for January 2005 taken from a previous simulation (see Zeng et al., 2015). The model is run using 34 levels, as it will be used operationally for satellite retrievals, where details of the pressure levels being given in Huijnen et al., 2010.

2.2 Emission inventories

All emission inventories applied in TM5-MP are yearly specific meaning that the year-to-year variability in emission fluxes due to changes in anthropogenic activity, biogenic activity and burning extent are taken into account. For the anthropogenic emission of NO_x, CO, SO₂, NH₃ and Non-Methane Volatile Organic Compounds (NMVOC), we adopt the MACCity emission estimates described in Granier et al. (2011). The lack of sector-specific information complicates the use of daily cycles for e.g. the road transport component, where a bi-sinusoidal distribution could be applied peaking in the morning and late afternoon to represent variability in traffic volume. Aircraft emissions are included only for NO, using a homogenous hourly flux estimate not related to regional flight times. For volcanic SO₂ emissions, the estimated emission flux has been scaled up to 10 Tg S yr⁻¹ based on Halmer et al. (2002). For the biogenic component, where available we use the CLM-MEGANv2.1 emission inventories produced for the Southern Hemispheric Multi-model Intercomparison Project (SHMIP) as described in Zeng et al. (2015), with the missing trace species (e.g. ethane, propane, higher organics) coming from alternative MEGAN simulations as outlined in Sindelarova et al. (2014). A diurnal cycle is imposed on the isoprene emissions and introduced into the first ~50m between 20°S-20°N, whereas for other latitudes a continuous daily flux is applied. The BB emissions are taken from the monthly estimates provided by the GFEDv3 inventory (van der Werf et al., 2010) and latitude dependent injection heights and a tropical burning cycle are implemented following Huijnen et al. (2010). All emission inventories are provided on a 0.5° x 0.5° resolution and subsequently coarsened onto the horizontal resolution employed in any

simulation. In TM5-MP all NO_x emissions are introduced as NO, rather than specifying a fraction that is emitted directly as NO_2 (Carslaw and Beevers, 2005). Global NO_x emissions for the year 2006 total 49 Tg N yr^{-1} (including lightning). Other notable species include CO (1081 Tg CO yr^{-1}), SO_2 (117 Tg S yr^{-1}), CH_2O (13.5 Tg C yr^{-1}) and isoprene (510 Tg C yr^{-1}). An overview of the global and zonal emissions terms used in the simulations analysed here are given in Table 3.

For lightning NO_x we use the parameterization which uses convective precipitation fields (Meijer et al., 2001) and constrain the annual global emission term at ~ 6 Tg N yr^{-1} . This uses the convective flux values meaning that re-scaling of the nudging term was necessary in order to achieve similar total lightning NO_x emissions across simulations. An example of the resulting horizontal distributions in lightning NO_x at ~ 400 hPa for the tropics for both horizontal resolutions is shown in the top panel of Fig. S1a in the supplementary material. Although the spatial variability increases at $1^\circ \times 1^\circ$, the global distribution remains essentially the same, where the constraints on annual lightning NO_x emissions homogenize the total emission flux between resolutions. One other factor affecting the vertical distribution of lightning NO_x emissions is the convective parameterization which is used. The lower panels of Fig. S1a show that, at this altitude, the Tiedke (1989) approach increases the NO_x emissions at this level by $\sim 14\%$, accompanied by a significant re-distribution between regions (c.f. SH below 30°S and a significant increase in the tropical component in the Tiedke simulation). However this is altitude dependent, where the absolute differences in the vertical distribution in the monthly NO_x emissions for a selection of latitudes are shown in Fig. S1b. Here comparisons are shown both over the continents (e.g. 50.5°N) and the oceans (e.g. 59.5°S). Although the differences in the integrated monthly global emission NO_x flux is only around $\sim 1\text{--}2\%$, the temporal and vertical distribution can be quite different between convective schemes. Profiles show that in the upper troposphere ERA-interim consistently results in higher NO_x emissions around 300hPa, especially for July.

Latitudinal constraints on CH_4 global distributions are applied using the methodology given in Banda et al. (2015) with a 3-day relaxation time. We also introduce similar constraints based on the appropriate surface measurements for H_2 in order to account for the latitudinal gradient and variability across seasons, which replaces the fixed global value of 550ppb used in previous versions. Finally, for Radon (Rn^{222}) emissions we apply the estimates of Schery (2004), whose global distribution is given in Zhang et al. (2011).

2.3 Observations

Although the performance of mCB05 in TM5 v3.0 has been validated for selected NMVOC, O_3 , CH_2O , CO and NO_y in both hemispheres (Williams et al., 2013; 2014; Fisher et al., 2015; Zeng et al., 2015), the significant changes made to both the chemical scheme and the rate parameters in mCB05v2 necessitate independent validation at both $3^\circ \times 2^\circ$ and $1^\circ \times 1^\circ$. We choose a range of ground-based and airborne measurements taken at diverse locations during the year 2006 representing different chemical regimes. Here we briefly describe the observations utilised for this purpose.

For validation of simulated surface concentrations we use measurements of gaseous O_3 , NO, NO_2 , HNO_3 and SO_2 available from the European Monitoring and Evaluation program (EMEP, www.emep.int), where we exploit measurements taken at various background sites in Norway, Finland, The Netherlands, Belgium, Poland, the Czech republic, Germany, Great Britain, Spain, Slovakia, Italy and Portugal. The number of sites

used for comparisons of trace species other than O_3 is smaller due to data availability. For the model composites we extract data from 3 hourly instantaneous output in order to assemble both the weekly and monthly mean values from the simulations. For the weekly comparisons of NO_2 and SO_2 we use values extracted at 13:00 local time, close to the overpass time of the OMI instrument (e.g. Boersma et al, 2008). The selected stations allow validation of the seasonality for both rural regions (FI37) and urban regions (NL09), where we include identical stations where possible for both species. For HNO_3 we assemble the weekly values from the daily averages.

Measured $[O_3]$ in the EMEP network are obtained using UV monitors (Aas et al. 2001). For all species, spatial interpolation of model data is performed accounting for the height of the measurement station and by weighting using the distance of the station from the surrounding grid-cells. The wide range of measurement sites chosen ensures that both background and polluted cases are assessed.

For validating the vertical distribution of relevant trace species such as O_3 , SO_2 and CH_2O , we use measurements by the DC-8 aircraft during the Intercontinental Chemical Transport Experiment B (INTEX-B; Singh et al., 2009) that took place between March and May 2006. Observations of a host of co-located nitrogen-containing species are available (namely NO , NO_2 , PAN and HNO_3). These flights were conducted over a wide region, and we use all three months of measurements. Each month sampled a different region representing different meteorological conditions and local emission sources, namely: the Gulf of Mexico (90-100°W, 15-30°N), the remote Pacific (176-140°W, 20-45°N) and to the south and west of Alaska over the ocean (160-135°W, 20-60°N). Measurements cover altitudes up to 10.5km, and we bin the values with respect to pressure using 50 hPa bins or less in the LT. We interpolated three-hourly output against measurements for each respective day, similar to the comparisons performed in previous evaluations of TM5 (e.g. Huijnen et al., 2010), but we segregate our comparisons into the three distinct regions. For details relating to the location of each flight the reader is referred to the campaign overview of Singh et al. (2009).

For tropospheric O_3 , we supplement the INTEX-B comparisons with measurements taken over more polluted regions as part of the Measurement of Ozone, water vapour, carbon monoxide and nitrogen oxides by Airbus In-service aircraft initiative (MOZAIC; Thouret et al., 1998). We aggregate the measurements as seasonal means for December-January-February (DJF) and June-July-August (JJA) in order to provide a robust number of samples for each location. Here we choose to use profiles representative of the Northern mid-latitudes, namely: London (0.2°W, 51.2°N), Vienna (16.5°E, 48.1°N), Washington (77.5°W, 38.9°N), Portland (122.6°W, 45.6°N), Shanghai (121.8°E, 31.2°N) and Tokyo (140.4°E, 35.8°N).

We also make comparisons of O_3 , NO , NO_2 , selected N-reservoir species, SO_2 and CH_2O profiles using measurements made aboard the NOAA WP-3D aircraft as part of the Second Texas Air Quality Study (TexAQS II; Parrish et al, 2009), which was conducted over the Texas sea-board during September and October 2006. This allows the assessment of TM5-MP over a region with higher NMVOC emissions and industrial activity. These measurements were typically sampled at altitudes below 500hPa, therefore no measurements in the UTLS are available from this campaign.

3 The Effect on Atmospheric Transport

Here we analyse the differences in convective transport out of the BL by analysing the vertical and horizontal distribution of ^{222}Rn , which is a diagnostic typically used for assessing the differences in transport in CTMs (e.g. Jacob et al., 1997). ^{222}Rn is emitted at a steady rate and exhibits a half-life of ~ 3.8 days, which is long enough to be transported from the BL into the FT due to chemical passivity, with loss via wet scavenging and dry deposition being negligible. Therefore, it acts as an ideal tracer to assess differences in convective transport from the surface out of the BL. The representation of BL dynamics for TM5-MP has recently been assessed at $1^\circ \times 1^\circ$ using ^{222}Rn distributions for both the Tiedtke (1989) scheme and when adopting convective mass transport values from the ERA-Interim meteorological data (Koffi et al, 2016).

Figure 1 shows seasonal mean horizontal global distributions of ^{222}Rn for DJF and JJA in the $1^\circ \times 1^\circ$ simulation averaged between 800 and 900hPa (i.e. sampling the LT). Also shown are the associated percentage differences against the re-binned $3^\circ \times 2^\circ$ ^{222}Rn distribution, allowing a direct comparison. Resolution dependent differences result from the cumulative effects of the use of higher resolution mass-fluxes from the ERA-interim meteorological data for describing convective activity and the more accurate temporal distribution of regional ^{222}Rn emissions at $1^\circ \times 1^\circ$. In general it can be seen that seasonal differences of $\pm 20\%$ exist, typically with increases over continents and decreases over oceans in the $1^\circ \times 1^\circ$ simulations. Maximum differences of $>60\%$ occur near selected coastal regions (California, West Africa, Madagascar) or in outflow regions such as off South America and Africa, where differences exhibit a strong seasonal dependency. This is due to the large differences in convective strength due to the variability in heating rates, and thus temperatures, between land and ocean (e.g. Sutton et al., 2007).

A comparison of the ratio of the monthly mean ^{222}Rn profiles ($1^\circ \times 1^\circ / 3^\circ \times 2^\circ$) extracted above selected European cities for January (black) and July (blue) 2006 are shown in Fig. S3 in the Supplementary Material. The typical tropospheric profile of ^{222}Rn exhibits an exponential decay from the LT to the FT (not shown). In order to homogenise the emission flux in the comparison, we coarsen the $1^\circ \times 1^\circ$ data onto the $3^\circ \times 2^\circ$ grid by averaging the six individual values into a representative mean column. The extent of the changes in the vertical distribution of ^{222}Rn is somewhat site specific meaning an in depth analysis is beyond the scope of this paper. In summary, the $1^\circ \times 1^\circ$ simulation generally provides stronger convective activity for January, with the main impact occurring below 700hPa (e.g. London and Paris). The changes in ^{222}Rn in the LT range between 2 and 10% (i.e. ratios of 0.9 to 1.1), implying both weaker and stronger convective transport depending on changes in location (e.g. orography and land type). The impact at Berlin is larger than e.g. Barcelona which shows that, surprisingly, the inclusion of a large ocean fraction (with weaker convective mixing) in the $3^\circ \times 2^\circ$ cell does not seem to introduce dominating effects. Recently Koffi et al. (2016) have shown that comparisons of ^{222}Rn at coastal sites in Europe at $1^\circ \times 1^\circ$ exhibit significant discrepancies compared to more continental stations. For July the changes in the vertical distribution extend into the FT up to 500hPa, although changes in the upper FT have a significant component due to changes in long-range transport. The magnitude of the changes are similar to those exhibited during January, although maybe of the opposite sign (e.g. Rome). Thus the influence on e.g. NO_2 , CH_2O and SO_2 *a-priori* vertical profiles will be non-negligible and diverse.

For the tropical cities located in regions where convective mixing is stronger, the corresponding differences between resolutions can reach $\pm 20\%$, especially near the surface (e.g. Caracas and Karachi). There is a site-specific seasonal dependency in the magnitude of the changes related to the regional land characteristics (e.g. Lagos versus Kuala Lumpur) and the extent of ocean within any particular grid-cell. Thus, differences in *a-*

priori vertical profiles of trace gases using a resolution of $1^\circ \times 1^\circ$ can be considerable compared to those provided at a $3^\circ \times 2^\circ$ resolution.

We also show ratios of profiles from $1^\circ \times 1^\circ$ simulations using the convective scheme of Tiedtke (1989) against those using the convective mass-fluxes from the ERA-interim meteorological dataset (Fig. S4), defined as $\text{ERA}(1^\circ \times 1^\circ)/\text{Tiedtke}(1^\circ \times 1^\circ)$. For this comparison no daily averaging is employed with ^{222}Rn profiles extracted from 3 hourly instantaneous sampling, with the profiles shown being interpolated directly above urban conurbations (with high trace gas emissions). The ratios show that the significant differences exist, with the convective mass-fluxes from ERA-interim being somewhat weaker than those calculated online using Tiedtke (1989) (i.e) the ratio is typically less than 1, especially during July. In the recent study by Koffi et al. (2016) performed at $1^\circ \times 1^\circ$ for the European domain, there was no appreciable improvement in the correlation co-efficients when distributions of ^{222}Rn were compared against measurements resulting in no strong conclusion towards which of the parameterizations results in better atmospheric transport.

4 The Impact on tropospheric photolysis frequencies

The changes in the spatio-temporal distribution of tropospheric clouds and surface albedo have the potential to alter the incident flux of photolysing light reaching the surface, and thus photochemical production and destruction terms. When present, clouds dominate the integrated optical density in the tropospheric column. TM5-MP uses a random overlap method for determining the impact of clouds on actinic flux, which is weighted by cloud cover (Williams et al., 2012). Comparing seasonal mean cloud coverage for DJF and JJA (Fig. S5), we show that there are significant increases in the fractional cloud cover (f_{cc}) at $1^\circ \times 1^\circ$ resulting in f_{cc} values ranging between 0.1-0.8 (c.f. 0.1-0.5 for $3^\circ \times 2^\circ$). Moreover, the definition of tropical equatorial cloud systems becomes much more defined and there are significant differences in the cloud distributions around the west coast of Southern America. For DJF, the largest changes occur at high latitudes over the tundra and oceans, but correspond with low intensity incident radiation due to the polar winter. For the SH, the seasonal f_{cc} increases significantly, which will potentially impose effects on Antarctic oxidative capacity (see Sect. 5). For JJA, most increases in f_{cc} do not occur directly above high NO_x sources but rather over the oceans. This limits the impact on the lifetime of chemical pre-cursors (e.g. NO_2) as discussed in Sect. 6. Examining similar plots for surface albedo (not shown) reveals that maximum differences (increases at $1^\circ \times 1^\circ$) again occur in the polar regions under low temperatures related to sea-ice and snow coverage typically during polar winters. For mid-latitudes and tropics, although differences in the absolute albedo value can be significant ($\pm 50\%$) values are typically below 0.1, which will contribute to the perturbations in the final J value tropospheric profiles as discussed below. The monthly mean comparisons in surface J values provided in Fig. S6 show that any differences in instantaneous cloud cover are moderated to the order of a few percent when looking at longer periods.

The similarity in the monthly mean photolysis frequencies for O_3 and NO_2 across resolutions (hereafter denoted J_{O_3} and J_{NO_2} , respectively) are shown in Fig. S6 of the Supplementary Material. Comparisons of the monthly mean J_{O_3} and J_{NO_2} values are shown at five different locations identical to those shown in Williams et al. (2012). For J_{O_3} the impact of increasing resolution is limited to a few percent in the monthly mean values, even for regions which have high surface albedo. At the global scale this leads to a reduction of $\sim 2\%$ in the

total mass of O_3 photolysed (not shown). For J_{NO_2} , the corresponding differences become more appreciable, with $1^\circ \times 1^\circ$ exhibiting ~5-10% higher values at high Northern latitudes (associated with locations with high- NO_x regimes). Focusing on J_{NO_2} and comparing seasonal mean values near the surface shows that very similar large-scale spatial patterns occur for both simulations at the global scale (c.f. Fig. S7). The highest J_{NO_2} values occur over the tropical oceans and high altitude regions (e.g. Nepal), with a latitudinal shift related to seasonal changes in daylight hours. Although more regional fine-structure can be seen at $1^\circ \times 1^\circ$ (e.g. South-Western US and South-West China for DJF), these seasonal averages show that the small perturbations in J_{NO_2} shown in Fig. S6 extend to the global scale, leading to only modest changes in the tropospheric lifetime of NO_2 (see Sect. 6).

Comparisons of monthly mean vertical profiles of J_{O_3} and J_{NO_2} as sampled over selected tropical cities are shown in the Figs. S8a and b, respectively, in the Supplementary Material. Here no averaging is performed towards an identical horizontal resolution, therefore values are representative of the J values directly above the selected urban centres. The J_{O_3} profiles are affected to a larger extent than the J_{NO_2} profiles, due to the characteristic absorption spectra of each species which makes J_{O_3} more sensitive to the additional scattering introduced due to clouds. Profiles over Dubai act as a proxy for clear-sky conditions, where values of unity exist in the residual of J_{O_3} and J_{NO_2} calculated through most of the column. The small difference at the surface is due to changes in the surface albedo between resolutions, with Dubai being situated on the coast meaning that a sharp horizontal gradient exists in surface albedo. For other cities, the largest perturbations occur away from the surface (e.g. Jakarta, Nairobi and Lagos) around the altitude where tropospheric clouds are most abundant. There are typically changes of between ± 5 -10% in the monthly mean profiles. The changes in J_{NO_2} reflect those simulated for J_{O_3} , with somewhat smaller perturbations.

5 Implications for oxidative capacity and tropospheric O_3

The partitioning of reactive N between the short- and long-lived chemical N-reservoirs included in TM5-MP depends on the oxidative capacity simulated for the troposphere via competition between the various different radicals (i.e. OH, $CH_3C(O)O_2$, NO_3 and CH_3O_2). Therefore, changes to the distribution and resident mixing ratios of tropospheric O_3 subsequently impose changes in the fractional composition of the NO_y budget (Olszyna et al., 1994) and also the efficiency of the NO_x recycling terms by altering the chain length (Lelieveld et al., 2004). In this section we analyse the global and zonal chemical budget terms for tropospheric O_3 to highlight the inter-hemispheric differences which occur (i.e. under low and high- NO_x environments). An overview of the resulting near-surface global distribution of tropospheric O_3 for May 2006 is shown in Figure 3, which also includes the location of the regional comparisons presented below in a larger global context. In general, the pattern of minimum and maximum mixing ratios in O_3 occur in similar locations, with the long-range transport component being more clearly defined in the $1^\circ \times 1^\circ$ simulation. There is a distinct latitudinal gradient in O_3 mixing ratios imposed by the global distribution of NO_x emissions.

Table 4 provides the zonally segregated chemical budget terms for tropospheric O_3 , from which the global component due to STE can be determined by closing the budget terms following the methodology given in Stevenson et al. (2006). The chemical tropopause calculated for $3^\circ \times 2^\circ$ is applied for the analysis of $1^\circ \times 1^\circ$ budget terms to ensure that a valid comparison is performed, (i.e. the same mass of air is accounted for). For

computational efficiency the budget terms are aggregated in 10° latitudinal bins for each vertical level and summed across all longitudes providing the cumulative latitudinal terms.

The most significant change with resolution concerns STE. By using a dedicated tagged stratospheric O_3 tracer (which only undergoes photo-chemical destruction and deposition in the troposphere; hereafter denoted as O_3S) changes in the zonal mean STE can be determined. The stratospheric burden of O_3 (BO_3 (strat)) exhibits a strong hemispheric gradient with much more downwelling occurring in the NH peaking during boreal springtime. At the global scale the STE exchange is $579 \text{ Tg } O_3 \text{ yr}^{-1}$, which agrees well with the multi-model mean for STE of $556 \pm 154 \text{ Tg } O_3 \text{ yr}^{-1}$ in Stevenson et al. (2006), with observational estimates being $\sim 550 \pm 140 \text{ Tg } O_3 \text{ yr}^{-1}$ (Olsen et al., 2001). The $\sim 7\%$ reduction of STE at $1^\circ \times 1^\circ$ is encouraging considering that previous studies using TM5 have concluded that STE in TM5 at $3^\circ \times 2^\circ$ was biased high compared to STE inferred from TES and MLS satellite observations (Verstraeten et al. (2015)). The increase in STE in the SH, with an associated decrease in the NH (see below), implies that there is a shift in circulation patterns at $1^\circ \times 1^\circ$ even though BO_3 (strat) remains essentially unchanged. Previous studies have shown that in order to resolve the correct spatial and temporal Stratosphere-Troposphere flux, high resolution is required both in the horizontal and the vertical gridding (e.g. Meloen et al., 2002). The NH STE diagnosed with TM5-MP is an order of magnitude smaller than estimates derived in a CTM study also conducted at a $1^\circ \times 1^\circ$ resolution (Tang et al, 2011; $\sim 200 \text{ Tg } O_3 \text{ yr}^{-1}$), which identified deep convection as important for STE. Here we use a different vertical grid and meteorological dataset to drive TM5-MP, both of which affect the ability towards capturing an accurate STE flux (Meloen et al., 2002). For the $1^\circ \times 1^\circ$ simulation using the Tiedtke scheme, there is a further reduction in the STE component of $21 \text{ Tg } O_3 \text{ yr}^{-1}$, resulting in an STE component almost identical to the multi-model mean in Stevenson et al. (2006).

The zonal seasonal means of the fraction of O_3S to O_3 (O_3S/O_3) for both simulations are shown in Fig. 2 for DJF and JJA. There is a clear seasonal zonal shift in the fractional contribution due to the O_3 transported downwards from the Stratosphere exhibiting a longer lifetime in the winter hemisphere reflecting a lower photochemical destruction rate. At $1^\circ \times 1^\circ$ the largest increase in STE occurs in the Southern Hemisphere (SH) during JJA. Here $\sim 20\text{-}25\%$ of tropospheric O_3 is transported down from the Stratosphere. Comparing the 0.2 contour for the NH mid-troposphere shows significant changes, extending further down towards the surface during boreal wintertime leading to the higher total mass of O_3S in the troposphere. The extent of nudging towards the MSR climatology is essentially constant across simulations (c.f. Table 4). Interestingly, less O_3S reaches the surface in the tropics at $1^\circ \times 1^\circ$ due to the enhanced chemical destruction term in the Free Troposphere. Approximately 10% of the global deposition term for O_3 is associated with O_3 that originates from the Stratospheric at $1^\circ \times 1^\circ$ (c.f. $\sim 5\%$ at $3^\circ \times 2^\circ$). For the NH, this contributes to the simulated increase in deposition of $\sim 9\%$.

For tropospheric O_3 there are similarities that occur between the NH, tropics and SH (i.e.) high and low- NO_x scenarios, resulting in a cumulative decrease in O_3 production of $\sim 2\text{-}4\%$ across zones. For the chemical loss terms there is a modest decrease of $\sim 3\%$ ($\sim 2\%$) in the NH (SH) reflective of the changes discussed for J_{O_3} , which acts as the primary destruction term. Therefore, in the SH the significant differences shown for f_{cc} do not significantly impose a lower photochemical destruction term on the annual tropospheric O_3 budget. There is a zonal gradient in the tropospheric burden of O_3 (BO_3) following the zonal gradient in NO_x emissions (c.f. Fig. 3). Comparing terms shows that BO_3 decreases at $1^\circ \times 1^\circ$ by a few percent at the global scale ($\sim 7 \text{ Tg } O_3$)

making a rather small impact on oxidative capacity. This is of the same order of magnitude as that found in previous studies concerned with horizontal resolution (e.g. Wild and Prather, 2006). Interestingly, changes in the deposition flux of O_3 are rather small, even though there is a larger amount of variability in the land surfaces and better-resolved land-sea contrast at $1^\circ \times 1^\circ$, although differences in regional deposition fluxes can be more significant. Multi-model inter-comparisons of surface deposition terms across models have shown previous versions of TM5 to be at the low end of the model spread in terms of O_3 (Hardacre et al., 2015), suggesting that the surface deposition flux should be increased by $\sim 10\%$ in TM5-MP towards the multi-model mean value. This can be partly attributed to the large uncertainty which exists related to the loss of O_3 to the ocean (Hardacre et al., 2015).

Figure 4 shows comparisons of simulated and observed mass mixing ratios of surface O_3 at EMEP sites across Europe (www.emep.int; Aas et al. 2001), with stations chosen to cover a range of latitudes. Previous comparisons using mCB05 have revealed high biases in surface O_3 , especially during boreal summertime (Williams et al., 2013). These high biases originate from cumulative effects associated with the accuracy of the emission inventories, the convective and turbulent mixing component, the underestimation of the scattering and absorption of photolysing light due to aerosols and the chemical mechanism that is employed. For the emission component it should be noted that even at $1^\circ \times 1^\circ$ coarsening is performed, where emission inventories are typically supplied at $0.5^\circ \times 0.5^\circ$ resolution. The seasonal cycle in surface O_3 is captured to a large degree, and the high bias exhibited by the model is generally reduced by $\sim 2\text{--}5$ ppb (or $\sim 20\%$) at $1^\circ \times 1^\circ$. This is associated with perturbations in the NO_x recycling terms, chemical titration by NO, changes to the turbulent diffusion and convective mixing out of the BL. In that the improvement in biases is largest during boreal summertime is associated with the shorter chain length of the NO_x recycling term during boreal wintertime. However, there is still a significant monthly mean bias in both simulations when compared against observations throughout the year, especially for locations impacted by a large anthropogenic NO_x source. This is partly due to the low NO/NO_2 ratio as discussed in Sect. 6 below.

Comparing vertical profiles from composites assembled from the MOZAIC measurements for DJF and JJA (Figs. S9a and S8b, respectively), INTEX-B (Singh et al, 2009; Fig. S10) and TexAQS II (Parrish et al, 2009; Fig. S11) show consistently that differences are small between simulations across regions, and typically mimic those which occur at the surface. There is a general positive bias of $\sim 20\text{--}40\%$ in mixing ratios exhibited across all comparisons, although the variability in the vertical gradients across regions is captured rather well. Such positive biases have consequences for both the NO_x recycling terms and HNO_3 formation discussed in the sections below.

6 Implications for the distribution of NO and NO_2

Table 5 provides the zonally segregated annual NO_x recycling terms involving the main peroxy-radicals and the direct titration term involving NO for the $1^\circ \times 1^\circ$ simulation. The conversion rate of NO back into NO_2 decreases by $\sim 2\text{--}3\%$ across zones as a consequence of an associated increase in the titration term and re-partitioning of N into long-lived reservoir species (see below). For the titration term involving NO, although the globally integrated flux remains relatively constant, there is contrasting behaviour for the two most important zones (TR, NH), which exhibit a lower and higher titration term, respectively. It has been shown that

for regions such as Europe the increased titration results in lower surface O_3 mixing ratios (c.f. Fig. 4), improving the boreal summertime high bias at the surface.

Important model uncertainties include the quality of the MACCity NO_x emission inventory, the lifetime of NO_2 simulated in TM5, BL mixing and the NO_x recycling term via the chemical titration of O_3 . Figure 3 provides an illustration of the global distribution in surface NO_2 during May 2006 for both the $3^\circ \times 2^\circ$ and $1^\circ \times 1^\circ$ simulations, where the short-lifetime means that the maximum mixing ratios occur directly near the strong source regions. Most NO_x is anthropogenic in origin, therefore there is strong latitudinal gradient between the NH and SH, with ship-tracks also visible. The regions where validation occurs are also superimposed in the figure, including the extent of the EMEP domain over which NO_2 weekly comparisons are made.

Figures 5 and 6 shows comparisons of weekly $[NO]$ and $[NO_2]$ surface measurements against the corresponding composites from both simulations, sampled at 13:00 local time which is close to the local overpass time for both OMI and tropOMI. Although the number of EMEP sites conducting NO_x measurements is smaller than those measuring O_3 , we choose stations located throughout Europe in both high and low NO_x regimes. To supplement these comparisons we provide the seasonal mean biases for DJF and JJA from both simulations in Tables 6 and 7, respectively, calculated using weekly binned data from all EMEP sites that measure hourly $[NO]$ and $[NO_2]$. Here we perform an analysis across sites rather than focusing on the behaviour at selected individual locations.

For the determination of $[NO_2]$, the reduction of NO on a Molybdenum convertor takes place with subsequent detection by chemi-luminescence, with an associated detection limit of ~ 0.4 ppb. Previous studies have shown that some bias can result due the oxidation of nitrogen reservoirs such as PAN (Dunlea et al., 2007; Steinbacher et al., 2007). In TM5-MP all NO_x emissions are introduced as NO, although a fraction for road transport is known to be emitted directly as NO_2 (e.g. Carslaw and Beevers, 2005). Many studies have been performed comparing satellite NO_2 columns with model values, implying that inadequacies in emission inventories are somewhat region specific (e.g. Zyrichidou et al., 2015; Pope et al., 2015).

Table 6 shows a negative bias of a few $\mu g\ m^{-3}$ in TM5-MP in seasonal surface $[NO]$ in Europe. This is a cumulative effect of the accuracy of the MACC NO_x emission estimates, an overestimate in daytime vertical mixing (Koffi et al., 2016) (enhanced dilution) and, to a lesser extent, too high surface $[O_3]$ (increasing the oxidation rate of NO to NO_2). As anthropogenic emissions are the principle source of NO, there is no significant seasonal cycle in the monthly emission estimates in the NH. Seasonal differences in convective mixing (i.e. lower BL heights) do cause somewhat higher surface $[NO]$ during DJF for approximately equal emission terms. This is captured by TM5-MP, although under night-time conditions TM5-MP has been shown to overestimate nocturnal BL heights (Koffi et al., 2016). For $\sim 80\%$ of the EMEP sites we do not observe any significant change in the quality of the comparisons. For $\sim 20\%$ of sites, simulations of $[NO]$ at $1^\circ \times 1^\circ$ introduce significant improvements over those at $3^\circ \times 2^\circ$ and there is an improvement regarding the extent of seasonal variability (Fig. 4).

Table 7 shows that for $[NO_2]$ the biases are more variable being typically in the range of $\pm 0-6\ \mu g\ m^{-3}$, with both positive and negative biases occurring across sites. Both the conversion efficiency from NO, loss to reservoir compounds (e.g. HNO_3), photo-dissociation rate, convective mixing and emission estimates contribute to these biases. The seasonal biases show improvements at $1^\circ \times 1^\circ$ for $\sim 35\%$ of the EMEP sites, accompanied with degradations at $\sim 20\%$ of the sites. The maximum biases in $[NO_2]$ at $1^\circ \times 1^\circ$ can be approximately double those

for [NO]. For the corresponding NO/NO₂ ratio, there will generally be an under prediction in the model due to the negative biases shown for the [NO] comparisons. Analyzing the corresponding seasonal correlation coefficients (not shown) shows in ~25% of the cases there is little seasonal correlation between the weekly [NO₂] in TM5-MP and the measurements regardless of resolution for both seasons (Pearson's r in the range -0.3 to 0.3). In ~30% of cases there is actually a degradation in r between resolutions, the changes somewhat reflect those seen in the seasonal biases i.e. simultaneous changes to both the meteorology and local emission fluxes do not necessarily improve the performance of the model. Comparing 1° x 1° values both with and without the Tiedtke convection scheme shows that for the most convective regions (e.g. south of 45°N) increases in r generally occur during JJA when employing the ERA-interim mass-fluxes. Conversely for e.g. Finland the correlation becomes worse.

Beyond Europe, we compared monthly mean TM5-MP vertical distributions of NO and NO₂ between March and May 2006 against measurements taken during the INTEX-B campaign in Fig. 7. In general differences between 1° x 1° and 3° x 2° simulations are the order of a few percent, with NO₂ biased low in the LT by ~70-80%. This is partially associated with the take-off and landing of the aircraft from polluted airfields, where point sources of high anthropogenic emissions cannot be resolved even at 1° x 1°. For March, there is a strong signature from biomass burning plumes in the middle troposphere which is not captured using the monthly burning estimates. For the FT, TM5-MP captures the observed gradient to reasonable degree. In the UT there is a consistent high bias for NO and an associated low bias for NO₂ suggesting that the conversion term is too low and the NO_x cycle is out of synch at these cold temperatures despite the addition of new reservoir species (i.e. CH₃O₂NO₂) and application of new rate data.

One important gauge as to whether the chemical mechanism can capture the correct recycling efficiency of NO into NO₂ is to examine their ratio, which is presented in the third column of Fig. 7. In the LT (< 900 hPa) NO/NO₂ ratios of 0.1-0.2 exist that are captured quite well by TM5-MP, with negligible differences between 3° x 2° and 1° x 1° simulations. For the FT, TM5-MP consistently overestimates the ratio in spite of a high bias in O₃ (c.f. Fig. 4) which is imposed by the overestimates in NO₂. This implies the chemical conversion is too slow and, assuming representative J_{NO_2} values, indicates a low bias in HO₂ or an under-estimation in the mixing ratios of other long-lived and short-lived NO_y compounds (see Sect. 7).

Finally in Fig. 8 we show the corresponding comparisons against measurements taken during the TexAQS II campaign (Parrish et al, 2009) for both September and October 2006. As for the EMEP comparisons shown in Figs. 5 and 6, there is a significant underestimation in NO and NO₂ mixing ratios, with both model profiles being outside the 1- σ variability in the observational mean. This is clearly related to the emission estimates for this region being underestimated in the current emission inventories (e.g. Kim et al., 2011). For the resulting NO/NO₂ ratio, TM5-MP captures the correct ratio in the lowest few hundred meters of the BL, but overestimates the ratio at higher altitudes as for more pristine environments, although there is marked improvement in the ratios simulated for October.

7 Changes in the NO_y budget

7.1 Long-lived reservoirs

The resolution dependent changes in the temporal distribution of $[\text{NO}_2]$, and associated differences in NMVOC chemical pre-cursor emissions have the potential to alter the partitioning of reactive NO_x between the three main chemical reservoirs included in mCB05v2 (i.e. HNO_3 , PAN and ORGNTR). The differences in both the deposition efficiency and tropospheric lifetimes between trace species at $1^\circ \times 1^\circ$ suggests that the fraction of NO_x that can be transported out of source regions could change significantly. Here we briefly examine the zonally integrated nitrogen budget terms between simulations to quantify the effect of applying a higher spatial resolution. The seasonal distribution of these three dominant reservoir species at $1^\circ \times 1^\circ$ and their individual contributions to total NO_y are shown in Figs. S12-S15 for DJF and JJA, respectively. Here we define NO_y as the cumulative total of NO , NO_2 , NO_3 , HNO_3 , PAN, $\text{CH}_3\text{O}_2\text{NO}_2$, HONO, $2^*\text{N}_2\text{O}_5$, lumped organic nitrates (ORGNTR) and HNO_4 . It should be noted that methyl-nitrate is not in this version of TM5-MP. These figures are provided as reference for the reader to aid understanding of the discussion below.

Table S1 in the Supplementary Material provides a zonal decomposition of the tropospheric chemical budget terms for HNO_3 , PAN and ORGNTR. For HNO_3 , even though the recent kinetic rate parameters increase (decrease) the chemical production term at the surface (UTLS) compared to older rate data (e.g. Seltzer et al., 2015), changes in the integrated column term are small. The changes at $1^\circ \times 1^\circ$ are somewhat latitude dependant (corresponding to low and high NO_x regimes), with only small increases occurring in the NH and associated decreases in the tropics related to lower $[\text{OH}]$ (i.e. chemical production). Loss by cumulative deposition terms only changes by a few percent, due to wet scavenging being so efficient for HNO_3 any associated change in the Surface Area Density (SAD) of cloud droplets (cm^2/cm^3) introduced by changes in the liquid water product

For PAN, both the production and destruction terms decrease marginally by $\sim 1\text{-}3\%$ across all zones, meaning the transport of NO_x out of the main source regions remains relatively robust. The total mass of N cycled through PAN is \sim four times that sequestered as HNO_3 , although the lifetime of PAN is shorter due the efficient thermal decomposition. The changes in the production term due to temporal increases in NO_2 near high NO_x source regions (c.f. Fig. 3) are partially offset by a reduction in the mixing ratios of the acetyl-peroxy radical (C_2O_3 in Table 1) due to e.g. increased dry deposition of organic precursors at $1^\circ \times 1^\circ$. Although the chemical budget terms only exhibit small changes, it can be expected that the global distribution of PAN is somewhat different due the changes in the convective and advective mixing due to the application of higher resolution meteorological data (c.f. Sect. 3).

For ORGNTR, there is a 5% reduction in the annual production term at $1^\circ \times 1^\circ$, with an associated decrease in the loss by deposition. Both the largest production and, thus, destruction terms occur in the tropics related to the strongest source of ORGNTR being biogenic pre-cursors in mCB05v2. Thus at $1^\circ \times 1^\circ$, this intermediate trace species becomes less important as a NO_x reservoir, .

Finally, the one additional intermediate not shown is $\text{CH}_3\text{O}_2\text{NO}_2$, which is primarily a stable vehicle for transporting NO_x from the surface up to the UTLS, where at cold temperatures it accounts for a significant fraction of NO_2 speciation along with HNO_4 (Browne et al., 2011). At the global scale three times as much nitrogen cycles through $\text{CH}_3\text{O}_2\text{NO}_2$ compared to PAN, although the thermal stability is low at temperatures $> 255^\circ\text{K}$ thus resident mixing ratios are typically small. This results in maximum mixing ratios occurring in the cold upper troposphere (up to ~ 0.2 ppb) and subsequently dissociates primarily by thermal decomposition (photolytic destruction accounting for $< 0.1\%$ of all destruction). At $1^\circ \times 1^\circ$ there is a few percent decrease in

the chemical production term as a result of lower CH_3O_2 mixing ratios and more variability in the temporal temperature distribution.

Comparisons of weekly $[\text{HNO}_3]$ at the surface in Europe are shown in Fig. 9 against measurements from the EMEP network. It has recently been determined that HNO_3 measurements are also sensitive to ambient night-time $[\text{N}_2\text{O}_5]$, which could result in a positive bias in the observations (Phillips et al., 2013). In general, the modelled seasonal cycle is not evident in the measurements, which exhibit a rather homogeneous variation in mixing ratios throughout the year typically, thus being somewhat decoupled from variability in photochemical activity. Comparisons show an underestimation in TM5-MP during March and an overestimation during JJA. No such seasonal pattern is observed for $[\text{NO}_2]$ (c.f. Fig. 6), thus seasonal $[\text{OH}]$ variability due to variations in photo-chemical activity and $[\text{H}_2\text{O}_{(\text{g})}]$ and/or an incorrect wash-out term which could both act as likely causes. The impact of resolution on $[\text{HNO}_3]$ is rather muted for most weeks resulting in no significant changes to the seasonal biases (not given), as constrained by the improvements in surface $[\text{NO}_2]$ (c.f. Fig. 6). The heterogeneous scavenging of HNO_3 into ammonium nitrate can act as a moderator toward gaseous HNO_3 . Although this heterogeneous conversion process is included in TM5-MP as described by the EQSAM approach, low concentrations of e.g. ammonium nitrate (not shown) typically result. Thus, gaseous $[\text{HNO}_3]$ remains too high due to too little conversion into particles and subsequent deposition.

For other regions outside Europe, we make comparisons of vertical profiles of HNO_3 and PAN between March and September 2006 against those measured during INTEX-B (Figure 10) and TexAQSII (Fig. S16). PAN is a good marker for transport in the free-troposphere due to the relatively long-lifetime at colder temperatures. For all regions the vertical gradients for both species are captured quite well, although some fine-structure is lost due to the vertical resolution of TM5-MP and insufficient pre-cursor emissions. This implies that the underestimation in NO_2 simulated in the UTLs (Fig. 7) is not due to insufficient transport of NO_2 away from source regions, but rather should be attributed to either missing chemistry or insufficient transport down from the stratosphere. Finally, for more polluted regions, the vertical gradient of HNO_3 is rather less steep than that observed, with significant low biases in the lower troposphere related to the low bias in NO_2 shown in Fig. 8. The impact of the $1^\circ \times 1^\circ$ resolution only results in a marginal improvement in the LT for HNO_3 (again similar to NO_2). For PAN the vertical profile in TM5-MP agrees remarkably well, although somewhat anti-correlated around 900hPa in both simulations and the rapid decrease in the lowest kilometre not being captured sufficiently. This overestimation would likely be larger if the emission estimates were increased as required to consolidate the NO_2 comparisons for the same campaign.

7.2 Short-lived reservoirs

Here we briefly discuss the perturbations introduced for the short-lived N-reservoirs, namely HONO, HNO_4 and N_2O_5 , where the chemical budget terms for all three species are provided in Table S2 in the Supplementary Material. For HONO it should be noted that many tropospheric CTMs have difficulty in simulating observed mixing ratios (e.g. Goncalves et al, 2012) suggesting missing (heterogeneous) source terms. The global production for HONO is an order of magnitude less than that for the other short-lived N-reservoirs. At $1^\circ \times 1^\circ$ there is ~10% more chemical production of HONO in high NO_x regions and no appreciable effect in low NO_x regions. Thus the impact of increased resolution on HONO production is rather small, which is surprising

considering the higher NO mixing ratios that occur in high NO_x regions (c.f. Fig 5). The muted response is due to competing oxidative processes, which effectively lower the OH available. For HNO₄, approximately the same mass of N cycles through this species as for PAN, although the shorter lifetime means that it is more important at regional scale. Again, the impact of resolution on this species is small, where decreases in [HO₂] result in no significant net change in production for the NH. The most significant changes occur for the global production and heterogeneous conversion of N₂O₅, with enhanced chemical production of ~12% at the global scale, increasing the heterogeneous sink term by ~6%, although the changes in the total mass of N converted are small. In general, this is due to an increase in the production of the NO₃ radical by ~10% at 1° x 1° (not shown) resulting in enhanced N₂O₅ mixing ratios.

8 Implications for tropospheric CH₂O retrieval

The implications of applying a higher resolution CTM for the global distribution of CH₂O are rather modest. Fig. S17 shows the near-surface global distributions of CH₂O for May 2006, where maximum mixing ratios occur near forested regions due to the link with isoprene oxidation (e.g. Palmer et al., 2006). The tropospheric lifetime of CH₂O is of the order of a few days, meaning that transport has little impact between simulations apart from in low emission areas. Also shown are the locations where regional validation occurs. In Table 8, we show zonally integrated chemical production and destruction terms for CH₂O, which suggests changes of the order of a few percent at the global scale. The most notable difference is the increase in the cumulative deposition term of ~4% at 1° x 1°, thus reducing the atmospheric lifetime of CH₂O in TM5-MP. Again, this low impact shows that the increase in the temporal variability of the meteorological data at 1° x 1°, and thus the local variability of cloud SAD, only changes the net deposition term by a few percent. Even though the temporal distribution of the surface mixing ratios shows more variability at 1° x 1° due to the better representation of regional pre-cursor sources terms (e.g.) isoprene and terpene, only moderate improvements occur to the simulated profiles and total columns due to changes in transport. For instance, when analysing individual production terms (not given) for the tropics, decreases are related to small changes in the dominating chemical source terms (e.g. oxidation of CH₃OOH; a reduction of ~3-5 Tg CH₂O yr⁻¹). For the chemical destruction term, the relative insensitivity of the photolysis of CH₂O towards resolution (similar to J_{O3}; c.f. Fig S4) results in small net decreases in line with changes in the chemical production term.

Figure 11 compares monthly mean tropospheric profiles of CH₂O measured during INTEX-B (Singh et al., 2009) with those from both TM5-MP simulations for March to May 2006. In general, there is a fair representation of the vertical gradient of CH₂O by TM5-MP for all months shown, although surface mixing ratios are typically too high suggesting loss by deposition to the ocean is underestimated (potentially related to underestimations in surface area due to lack of 3D wave structure) or that the chemical production term is too efficient. Moreover, there appears to be a missing (chemical) source term in the UTLS in TM5-MP leading to a ~ 30-50% (~0.05 ppb) low bias above 600hPa, i.e. there is no significant improvement to the underestimation in the SH CH₂O column in TM5-MP when compared to mCB05 (Zeng et al, 2015). Comparing profiles shows that the changes in the vertical distribution of CH₂O at 1° x 1° are minimal in the chemical background compared to 3° x 2°, with the main differences originating from more efficient transport out of source regions

(c.f. March). These findings are further confirmed by the comparisons of TM5-MP against TexAQS II measurements for September and October 2006 (Fig. S18).

9 Implications for tropospheric SO₂ retrieval

The global distribution of near-surface SO₂ mixing ratios for both the 3° x 2° and 1° x 1° simulations are shown in the bottom panels of Fig. S17, where the distribution shows the land-based point sources as applied from the MACCity emission inventory. The high mixing ratios of SO₂ correlate with the location of strong anthropogenic emission sources due to the relatively short atmospheric lifetime of SO₂ (varying between ~2 days during winter and ~19 hours during summer (Lee et al, 2011)), being rapidly oxidized to sulphate (SO₄²⁻). Although the regional distributions are similar, the 1° x 1° simulation is able to differentiate point sources to a much better degree, which enhances the ability of deriving more accurate emission fluxes. The *in-situ* chemical production term of SO₂ from the oxidation of oceanic di-methyl sulphide (DMS) is low thus there are very low SO₂ mixing ratios in the chemical background. Also shown are the regions used for validating the SO₂ surface concentrations and vertical profiles (insets in FigS17; see below).

In Figure 12, we compare weekly [SO₂] for 2006 at a number of EMEP sites in Austria (AT02, forested), The Netherlands (NL09, rural), Great Britain (GB43, rural) and Spain (ES10, rural), with most sites being positioned away from strong point sources. For SO₂ in Europe, the main emission source is anthropogenic (e.g. from the energy sector). High [SO₂] has been observed throughout the EMEP network in e.g. The Netherlands and Spain, which is significantly higher than that measured in Central Europe (Tørseth et al., 2012). Although the measurement uncertainty is somewhat site specific due to the different methodologies employed, it is typically around ~1.3 ug/m³ (e.g. Hamad et al., 2010). Comparing weekly averages shows that for most sites shown there is a significant low bias at 3° x 2°, indicating inaccuracies in the MACC emission inventory and the effect of coarsening to the model resolution. At 1° x 1° significant improvements occur in the correlations as a result of the better temporal distribution of anthropogenic emission sources.

Table 9 provides an overview of the seasonal biases for all of the EMEP sites that measure hourly [SO₂], with the biases calculated for the overpass time of tropOMI aggregated on a weekly basis. Improvements occur at 1° x 1° for ~20% of the sites during both seasons, with the majority (~50%) of sites showing no significant improvement (< 5%). In such instances the local [SO₂] is determined more by long-range transport (thus sensitive to wash-out) rather than a local emission source, where strong mitigation practises have been implemented in Europe over the last few decades reducing resident [SO₂] significantly (Tørseth et al., 2012). For some sites there is a notable increase in biases at 1° x 1° (20% DJF, 25% JJA) indicating that too strong local emission sources occur in the MACC inventories (e.g. ES13 and GR01). For others (e.g. ES08 and NL07) significantly low biases occur suggesting the opposite problem.

Finally, for the vertical profiles, we make comparisons against monthly mean composites assembled from measurements taken during INTEx-B (Fig. S19) and TexAQS II (Fig. 13) as for the other trace gas species. For the more pristine locations there are typically low biases at 3° x 2° for all months, especially at the surface during March indicating a significant underestimation in the emission fluxes of SO₂. Increasing to 1° x 1° only provides an improved correlation for March, due to the transport in the FT being described better as shown for NO₂ in Fig. 7. For April, the comparison shows a significant underestimation in the column for both

simulations, where corresponding comparisons of the vertical profiles of DMS, which acts as a key source of SO₂ in the Equatorial Pacific (Alonza Gray et al., 2011), agree quite well (not shown). This points to an appreciable biogenic source term that is currently missing from the inventories as proposed for organic nitrates (Williams et al., 2014). For May again no significant improvement occurs at 1° x 1°, although both simulations capture the peak in SO₂ mixing ratios at the top of the BL. More relevant for satellite based retrievals is the observed column near strong anthropogenic source regions as shown in Fig. 13 over Texas during September and October 2006. Here a clear improvement occurs at 1° x 1°, with the low bias in the BL being reduced significantly although the integrated column is still too low. Again this is due to the underestimation in the source emission fluxes in the anthropogenic emission inventory employed.

10 Conclusions

In this paper we have provided a comprehensive description of the high-resolution 1° x 1° version of TM5, which is to be used for the purpose of providing *a-priori* columns for the satellite retrieval of trace gas columns of NO₂, CH₂O and SO₂. By performing identical simulations at a horizontal resolution of 3° x 2° and 1° x 1°, and comparing the resulting global distributions of trace gas species, photolysis frequencies and chemical budget terms, we quantify and validate both the near-surface and vertical distributions for the evaluation year of 2006.

Comparing the seasonal distribution in ²²²Rn between resolutions we show differences in the vertical distribution of up to ±20% at the global scale, with significantly larger impacts for specific coastal regions and tropical oceans. In order to assess the changes in convective activity above strong NO_x sources, we show that differences of between ~2-10% (~10-20%) exist for the Northern mid-latitudes (tropics) at higher resolution, with both weaker and stronger upwelling occurring depending on the region and the season. The magnitude of the changes are site specific being affected by local orography. We have also made comparisons using a 1° x 1° simulation applying the Tiedtke (1989) convection scheme, showing that ERA-interim mass-fluxes result in less transport of ²²²Rn out of the boundary layer, where it has been shown that the use of ERA-interim mass-fluxes introduces inconclusive improvements in surface ²²²Rn distributions (Koffi et al., 2016).

Although the impact of resolution on daily photolysis rates maybe appreciable, analysing global monthly mean J_{O_3} and J_{NO_2} surface values over a range of conditions shows that effects are limited to ~2% and ~5-10%, respectively. One contributing factor to this rather muted impact is that the changes in surface albedo that occur at 1° x 1° are largest at the poles during winter, which has no impact on photo-chemistry due to the absence of photolysing light (not shown). For cloud cover, a dominant term for determining total optical depth, there are significant increases at 1° x 1° over the oceans, although generally related to instances of low photochemical activity. Examining the resulting changes in J_{O_3} and J_{NO_2} which occur throughout the tropospheric column reveals that significant differences of >10% can occur at the top of the BL at tropical locations. Such modest changes associated with this dominant loss term result in the change in the integrated chemical budget terms for tropospheric O₃ and NO₂ to be rather low.

Analysing the chemical budget terms for tropospheric O₃ shows (i) a reduction in the stratosphere-troposphere exchange flux of ~7% to 597 Tg O₃ yr⁻¹, (ii) a repartitioning of the contribution from stratospheric downwelling in both the Northern and Southern hemispheres, (iii) no significant change in the tropospheric burden

of O_3 and (iv) modest changes in the integrated chemical production and destruction terms. Comparing simulated mixing ratios against surface measurements in Europe shows that the positive bias present in TM5 decreases by ~20% at $1^\circ \times 1^\circ$ between 2-5 ppb/month. This positive bias persists throughout the vertical column across diverse global regions regardless of the local NO_x emissions, although the vertical gradient in tropospheric O_3 through the tropospheric column is captured quite well.

For NO and NO_2 increasing horizontal resolution results in only modest differences in the zonal mean recycling terms and the loss of O_3 by chemical titration. Comparisons against surface measurements in Europe shows that there is a consistent negative bias in weekly [NO] of a few $\mu g\ m^{-3}$ associated with both too high surface O_3 (enhanced NO titration) and the inaccuracy of the NO_x emission inventories. For NO_2 , the biases in the weekly concentrations are larger and can be both positive and negative. Increasing horizontal resolution has little effect on reducing the NO biases, but results in improvements for NO_2 at ~35% of the available sites, with ~45% of sites showing limited changes. Examining correlation co-efficients shows that although there is typically a higher correlation at $1^\circ \times 1^\circ$, many sites still exhibit very low correlation or anti-correlation for some seasons. For the tropospheric column the improvement in the comparisons is only by a few percent, with a significant underestimation in both NO and NO_2 throughout the tropospheric column. Analysing the NO/ NO_2 ratio and comparing against observations shows that although partitioning is captured in the BL there is a significant overestimation in the upper troposphere.

Finally for CH_2O and SO_2 , which can also be retrieved from satellite measurements, the effect of increased resolution is rather modest due to compensating changes towards the chemical budget terms. When compared against observations there is a persistent low bias for tropospheric CH_2O due to missing production terms especially on the Free Troposphere. For SO_2 comparison with surface observations in Europe shows lower biases at 20% of sites due to more accurate local emission fluxes, whereas for the majority of cases (~50%) there is no significant change. Comparing vertical profiles shows a significant underestimation in the tropospheric column likely associated with either missing precursors or an underestimation in the direct emission terms.

Future updates to TM5-MP will most likely focus on developing an online Secondary Organic Aerosol scheme, tropospheric halogen chemistry and incorporating an updated isoprene oxidation scheme involving more intermediate species. It will also be applied in the context of an Earth System Model (EC-EARTH) for allowing future studies concerning chemistry-climate feedbacks. When computing resources allow more expensive simulations can be performed using the 60 vertical levels as defined in the ERA-Interim meteorological dataset, approximately doubling the resolution of the simulations presented here. An additional update to improve the STE would be to apply the second-order moments scheme (Prather, 1986), whose application has been shown to capture the seasonality and magnitude of STE exchange to a better degree (Bönisch et al., 2008). In terms of oxidative capacity, one means of reducing the tropospheric near-surface O_3 mixing ratios would be improve loss to land-surfaces (Hardacre et al., 2010), although mixing ratios have been shown to be insensitive to the additional loss term to oceans, which is currently missing from many CTM's (Ganzeveld et al., 2009). Our comparisons of CH_2O and SO_2 show that there is a significant uncertainty of chemical processes that affect distributions in the pristine marine environment. For instance, the physical process of deposition seems to be under-represented possibly due to too low surface area of the surface i.e. lack

of a flat surface. The significant underestimates in SO₂ suggest missing biogenic sources terms, therefore more understanding of biogenic emission terms is necessary.

Code Availability

The TM5-MP code can be downloaded from the SVN server hosted at KNMI, The Netherlands. A request to generate a new user account for access can be made by e-mailing sager@knmi.nl. Any new user groups need to agree to the protocol set out for use, where it is expected that any developments are accessible to all users after publication of results. Attendance at 9-monthly TM5 international meetings is encouraged to avoid duplicity and conflict of interests.

Acknowledgements

This research has been supported by FP7 project Quality Assurance for Essential Climate Variables (QA4ECV), no. 607405. We thank M. van Weele for processing the MSR2 stratospheric ozone data record used for constraining the overhead O₃ field and T. P. C. van Noije for updating the SO_x emission estimates. We thank V. Huijnen for providing estimates on the heterogeneous uptake co-efficients.

851 Table 1: Details of the reaction rate data applied for NO_x and nitrogen reservoirs. The k₀ terms are multiplied by
 852 the relevant air density to calculate the correct forward and backward rate constants. The reaction data and
 853 stoichiometry are taken from Atkinson et al. (2004) accommodating the latest evaluation at [http://iupac.pole-](http://iupac.pole-ether.fr)
 854 [ether.fr](http://iupac.pole-ether.fr).

Reactants	Products	Rate parameters
NO + O ₃	NO ₂	$3.0 \times 10^{-12} \cdot \exp(-1500/T)$
NO ₂ + O ₃	NO ₃	$1.4 \times 10^{-13} \cdot \exp(-2470/T)$
NO + HO ₂	NO ₂ + OH	$3.3 \times 10^{-12} \cdot \exp(270/T)$
NO + CH ₃ O ₂	CH ₂ O + HO ₂ + NO ₂	$2.8 \times 10^{-12} \cdot \exp(300/T)$
OH + NO ₂	HNO ₃	$k_0 = 3.2 \times 10^{-30} \cdot (300/T)^{4.5}$ $k_\infty = 3.0 \times 10^{-11}$
NO + NO ₃	NO ₂ + NO ₂	$1.8 \times 10^{-11} \cdot \exp(110/T)$
NO ₂ + NO ₃	N ₂ O ₅	$k_0 = 8.0 \times 10^{-27} \cdot (300/T)^{3.5}$ $k_\infty = 3.0 \times 10^{-11} \cdot (300/T)^{1.0}$
N ₂ O ₅ + M	NO ₂ + NO ₃	$k_0 = 1.3 \times 10^{-3} \cdot (300/T)^{3.5} \cdot \exp(-11000/T)$ $k_\infty = 9.7 \times 10^{14} \cdot (300/T)^{-0.1} \cdot \exp(-11080/T)$
HO ₂ + NO ₂	HNO ₄	$k_0 = 1.4 \times 10^{-31} \cdot (300/T)^{3.1}$ $k_\infty = 4.0 \times 10^{-12}$
HNO ₄ + M	HO ₂ + NO ₂	$k_0 = 4.1 \times 10^{-5} \cdot \exp(-10650/T)$ $k_\infty = 6.0 \times 10^{15} \cdot \exp(-11170/T)$
OH + HNO ₄	NO ₂	$1.3 \times 10^{-12} \cdot \exp(380/T)$
OH + NO + M	HONO	$k_0 = 7.0 \times 10^{-31} \cdot (300/T)^{4.4}$ $k_\infty = 3.6 \times 10^{-11} \cdot (300/T)^{0.1}$
HONO + hν	OH + NO	
OH + HONO	NO ₂	$2.5 \times 10^{-12} \cdot \exp(260/T)$
NO ₂ + CH ₃ C(O)O ₂	PAN	$k_0 = 3.28 \times 10^{-28} \cdot (300/T)^{6.87}$ $k_\infty = 1.125 \times 10^{-11} \cdot (300/T)^{1.105}$
PAN	NO ₂ + CH ₃ C(O)O ₂	$k_0 = 1.1 \times 10^{-5} \cdot \exp(-10100/T)$ $k_\infty = 1.9 \times 10^{17} \cdot \exp(-14100/T)$

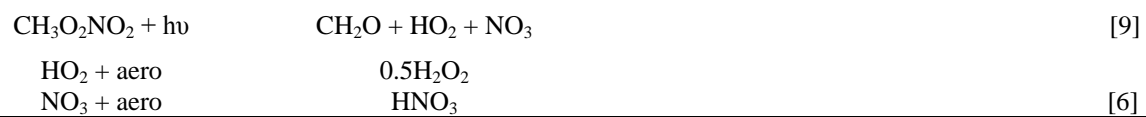
PAN + hν	CH ₃ C(O)O ₂ + NO ₂	
	CH ₃ O ₂ + NO ₃	
CH ₃ O ₂ + NO ₂	CH ₃ O ₂ NO ₂	k ₀ = 2.5 x 10 ⁻³⁰ *(300/T) k _∞ = 1.8 x 10 ⁻¹¹
CH ₃ O ₂ NO ₂	CH ₃ O ₂ + NO ₂	k ₀ = 9.0 x 10 ⁻⁵ *exp(-9690/T) k _∞ = 1.1 x 10 ¹⁶ *exp(-10560/T)
NO ₃ + HO ₂	HNO ₃	4.0 x 10 ⁻¹²

855

856

Table 2: Details of updates made to the reaction data and stoichiometry of the modified CB05 chemical mechanism for other reactions. Data is taken from the following: [1] Atkinson et al. (2004) accommodating the latest evaluation at <http://iupac.pole-ether.fr>, [2] branching ratio (R) equal to $1/(1+498 \cdot \exp(-1160/T))$, [3] Yarwood et al. (2005), [4] Sander et al. (2011), [5], Atkinson et al. (2006), [6] Emmons et al. (2010), [7] Hauglustaine et al. (2014), [8] rate assumed equal to NH_2 analogue, [9] assumed to be equal to HNO_4 after Browne et al. (2011) and E is an estimated value.

Reactants	Products	Rate expression	Ref.
$\text{CH}_3\text{O}_2 + \text{HO}_2$	CH_3OOH	$3.8 \times 10^{-13} \cdot \exp(750/T) \cdot R$	[1],[2]
$\text{CH}_3\text{O}_2 + \text{HO}_2$	CH_2O	$3.8 \times 10^{-13} \cdot \exp(750/T) \cdot (1-R)$	[1],[2]
$\text{CH}_3\text{O}_2 + \text{CH}_3\text{O}_2$	$1.37\text{CH}_2\text{O} + 0.74\text{HO}_2 + 0.63\text{CH}_3\text{OH}$	$9.5 \times 10^{-14} \cdot \exp(390/T)$	[3],[4]
$\text{OH} + \text{C}_3\text{H}_8$	$i\text{-C}_3\text{H}_7\text{O}_2$	$7.6 \times 10^{-12} \cdot \exp(-585/T)$	[5],[6]
$\text{NO} + \text{IC}_3\text{H}_7\text{O}_2$	$0.82\text{CH}_3\text{COCH}_3 + \text{HO}_2 + 0.27\text{ALD2} + \text{NO}_2$	$4.2 \times 10^{-12} \cdot \exp(180/T)$	[6]
$\text{HO}_2 + \text{IC}_3\text{H}_7\text{O}_2$	ROOH	$7.5 \times 10^{-13} \cdot \exp(700/T)$	[6]
$\text{OH} + \text{C}_3\text{H}_6$	$\text{C}_3\text{H}_6\text{O}_2$	$k_0 = 8.0 \times 10^{-27} \cdot (-300/T)^{3.5}$ $k_\infty = 3.0 \times 10^{-11} \cdot (-300/T)^{1.0}$	[5],[6]
$\text{NO}_3 + \text{C}_5\text{H}_8$	$0.2\text{ISPD} + \text{XO}_2 + 0.8\text{HO}_2 + 0.8\text{ORGNTR} + 0.8\text{ALD2} + 2.4\text{PAR} + 0.2\text{NO}_2$	$2.95 \times 10^{-12} \cdot \exp(465/T)$	[5]
$\text{NO} + \text{C}_3\text{H}_6\text{O}_2$	$\text{ALD2} + \text{CH}_2\text{O} + \text{HO}_2 + \text{NO}_2$	$4.2 \times 10^{-12} \cdot \exp(180/T)$	[6]
$\text{HO}_2 + \text{C}_3\text{H}_6\text{O}_2$	ROOH	$7.5 \times 10^{-13} \cdot \exp(700/T)$	[6]
$\text{NO}_3 + \text{DMS}$	$\text{SO}_2 + \text{HNO}_3$	$1.9 \times 10^{-13} \cdot \exp(520/T)$	[1]
$\text{NH}_2 + \text{OH}$		3.4×10^{-11}	[E]
$\text{NH}_2 + \text{HO}_2$	NH_3	3.4×10^{-11}	[4],[7]
$\text{NH}_2 + \text{O}_3$	NH_2O_2	$4.3 \times 10^{-12} \cdot \exp(-930/T)$	[4],[7]
$\text{NH}_2 + \text{O}_2$	NO	6.0×10^{-21}	[1],[7]
$\text{NH}_2\text{O}_2 + \text{NO}$	$\text{NH}_2 + \text{NO}_2$	$4.0 \times 10^{-12} \cdot \exp(450/T)$	[7],[8]
$\text{NH}_2\text{O}_2 + \text{O}_3$	NH_2	$4.3 \times 10^{-12} \cdot \exp(-930/T)$	[7],[8]
$\text{NH}_2\text{O}_2 + \text{HO}_2$	NH_2	3.4×10^{-11}	[8]
$\text{CH}_3\text{O}_2\text{NO}_2 + h\nu$	$\text{CH}_3\text{O}_2 + \text{NO}_2$		[9]



864

865

Table 3: The zonally segregated emission totals introduced into TM5-MP for the year 2006. All organic hydrocarbons are given in Tg C yr⁻¹, except for CO (Tg CO yr⁻¹), CH₂O (Tg CH₂O yr⁻¹) and CH₃OH (Tg CH₃OH yr⁻¹). All NO_x emissions are introduced as NO (Tg N yr⁻¹). For SO₂ emission totals are given as Tg SO₂ yr⁻¹ and for NH₃ as Tg NH₃ yr⁻¹. No direct emissions occur for HNO₃, PAN, ORGNTR, HONO, N₂O₅, NO₂, CH₃O₂NO₂ or O₃.

Species Tg Yr ⁻¹	Global	30-90°S	30S-30°N	30-90°N
CO	1081.0	24.4	755.1	301.27
NO _x (as N)	49.0	1.5	24.0	23.6
SO ₂	117.0	3.0	49.2	64.3
DMS (as S)	19.2	6.7	9.3	3.2
NH ₃	56.6	3.1	27.9	25.6
CH ₂ O	13.5	0.3	10.5	2.7
PAR	34.1	0.7	18.5	14.9
OLE	22.4	0.9	16.6	4.9
ALD2	13.4	0.4	11.2	1.8
CH ₃ CHCHO	2.2	0.0	1.2	1.0
CH ₃ OH	100.7	3.3	82.5	14.9
CH ₃ CH ₂ OH	70.4	2.8	52.6	15.1
C ₂ H ₄	25.9	1.0	19.0	5.9
C ₂ H ₆	6.1	0.3	5.3	1.5
C ₃ H ₈	5.6	0.4	3.6	1.6
C ₃ H ₆	19.6	0.9	14.8	3.9
CH ₃ COCH ₃	27.4	0.8	22.0	4.6
HCOOH	1.8	0.0	1.5	0.3
CH ₃ COOH	7.1	0.1	6.0	1.0
C ₅ H ₈	510.0	23.2	441.9	45.0
C ₁₀ H ₁₆	85.4	2.3	70.2	12.9

Table 4: The tropospheric chemical budget terms and burden for O₃ during 2006 for the 1° x 1° simulation, with all quantities being given in Tg O₃ yr⁻¹. The associated percentage changes are given when comparing against the 3° x 2° simulation (equal to (1° x 1°)-(3° x 2°)/3° x 2°). The definition of the chemical tropopause and the calculation of the STE are calculated using the methodology outlined in Stevenson et al. (2006). The stratospheric nudging term refers to total change in the mass of O₃ in the stratospheric column when constraining zonal distributions towards observational values from the MSR (Huijnen et al., 2010). The contribution to each term from the SH extra-tropics/tropics/NH extra-tropics regions (defined as 90-30°S/30°S-30°N/30-90°N) are provided.

Term	Global	%	SH	%	Tropics	%	NH	%
Net STE	579	-6.7						
Strat. Nudging	1440	-0.7	-224	2.8	1615	-	49	5.8
Trop.Chem.Prod	5532	-1.9	389	-2.2	3938	-3.5	1206	-2.2
Trop.Chem.Loss	5162	-2.4	440	-1.0	3869	-2.5	853	-2.8
BO ₃	378	-2.0	72	1.7	203	-2.3	104	-3.4
Strat BO ₃	80	-2.0	23	9.1	38	-6.5	24	-2.0
Deposition	949	0.8	115	0.6	465	-	369	1.9
O ₃ S Deposition	97	5.0	19	7.5	37	-1.2	42	10.0

Table 5: The annual NO to NO₂ re-cycling terms involving peroxy-radicals given in Tg N yr⁻¹ for 2006 at 1° x 1° resolution. In mCB05v2 XO₂ represents lumped alkyl-peroxy radicals (Yarwood et al, 2005). The NO + RO₂ term is an aggregate of numerous specific peroxy-radical conversion terms in the modified CB05 mechanism (Williams et al., 2013; Tables 1 and 2). Also provided are the approximate percentage differences when comparing with 3° x 2° (equal to (1° x 1°)-(3° x 2°)/3° x 2°). The chemical tropopause is defined using the methodology outlined in Stevenson et al. (2006).

Reaction	Global	%	SH	%	Tropics	%	NH	%
NO + HO ₂	1058	-1.2	79	-1.2	740	-1.9	239	-1.8
NO + CH ₃ O ₂	407	-2.2	31	-2.6	294	-2.8	82	-2.5
NO + XO ₂	147	-2.1	7	-3.6	111	-2.6	29	-2.6
NO + RO ₂	9.4	-4.4	0.4	-2.6	6.3	-4.4	2.7	-4.7
NO + O ₃	5403	0.1	518	7.5	2933	-3.9	1953	-4.9

Table 6: The seasonal mean absolute biases as calculated using weekly [NO] values ($\mu\text{g m}^{-3}$). The weekly means are composed from daily measurements taken at 13:00 for DJF and JJA (given as the difference in the measurements-model). Values are shown for both the $3^\circ \times 2^\circ$ and $1^\circ \times 1^\circ$ simulations for all stations with available data. Those with differences $< 5\%$ are considered to exhibit no discernible change in the bias.

EMEP Station	Lat	Lon	DJF $3^\circ \times 2^\circ$	DJF $1^\circ \times 1^\circ$	JJA $3^\circ \times 2^\circ$	JJA $1^\circ \times 1^\circ$
CH01	46.32	7.59	-0.01	-0.01	0.00	-0.01
CZ03	49.35	15.50	-4.05	-3.30	-1.61	-1.35
DE43	47.48	11.10	-2.37	-2.36	-0.47	-0.48
DK05	54.44	10.44	-2.51	-2.61	-1.29	-1.51
ES07	58.23	21.49	-3.80	-3.84	-1.45	-1.48
ES08	43.26	-4.51	-2.08	-2.09	-1.00	-1.01
ES09	41.16	-3.80	-0.93	-0.93	-1.07	-1.07
ES10	38.28	3.19	-1.14	-1.24	-0.75	-0.88
ES11	39.50	-6.55	-1.07	-1.07	-0.44	-0.45
ES12	41.17	-1.60	-1.34	-1.34	-0.95	-0.95
ES13	41.24	-5.52	-2.50	-1.90	-0.74	-0.62
ES14	39.31	0.43	-2.21	-2.20	-1.27	-1.27
ES15	43.13	-4.21	-1.62	-1.61	-0.99	-1.00
ES16	43.37	-7.41	-2.39	-2.39	-1.11	-1.11
FR13	46.39	0.11	-1.90	-1.94	-0.52	-0.52
FR15	55.18	0.45	-3.09	-3.04	-1.51	-1.58
GB02	50.35	-3.12	-1.23	-1.23	-0.93	-0.92
GB13	54.20	-3.42	-1.28	-1.32	-0.58	-0.55
GB14	52.30	-0.48	-3.03	-3.04	-0.98	-0.98
GB31	53.23	-3.11	-1.74	-1.74	-0.90	-0.91
GB37	50.47	-1.45	-3.09	-3.08	-1.22	-1.21
GB38	51.13	0.10	-2.87	-2.78	-1.92	-1.72
GB44	51.17	-3.20	-1.65	-1.45	-0.27	-0.67
GB45	52.17	0.17	-1.80	0.11	0.20	0.19
GB51	52.33	0.46	-3.68	-3.42	-1.29	-1.17
NL91	52.18	4.30	-4.47	-3.51	-1.98	-1.86

910 Table 7: As for Table 5 except for NO₂.
 911

EMEP Station	Lat	Lon	DJF 3° x 2°	DJF 1° x 1°	JJA 3° x 2°	JJA 1° x 1°
BE32	50.30	4.59	10.56	1.27	1.69	-2.13
CH01	46.32	7.59	-0.04	-0.03	-0.02	-0.01
CZ03	49.35	15.50	-4.04	0.03	-1.62	0.34
DE43	47.48	11.10	-2.37	-2.36	-0.49	-0.48
DK05	54.44	10.44	6.07	5.56	1.04	-0.02
ES07	58.23	21.49	-1.13	-1.79	-0.96	-1.15
ES08	43.26	-4.51	-2.01	-2.10	-0.93	-1.01
ES09	41.16	-3.80	-0.95	-0.94	-1.07	-1.07
ES10	42.19	3.19	2.18	1.46	0.92	-0.01
ES11	38.28	-6.55	-1.08	-1.08	-0.44	-0.44
ES12	39.50	-1.60	-1.36	-1.35	-0.95	-0.95
ES13	41.17	-5.52	-2.51	-0.29	-0.74	0.19
ES14	41.24	0.43	-2.22	-2.21	-1.27	-1.26
ES15	39.31	-4.21	-1.64	-1.63	-0.99	-0.99
ES16	43.13	-7.41	-2.40	-2.39	-1.11	-1.11
FI09	59.46	21.22	0.79	-0.91	-0.10	-0.53
FI37	60.31	27.41	10.04	9.60	1.70	0.92
FI96	62.35	24.11	0.40	0.34	0.31	0.17
FR13	43.37	0.11	-1.96	-1.95	-0.54	-0.54
FR15	46.39	0.45	-3.84	-3.91	-1.78	-1.81
GB02	55.18	-3.12	3.12	3.42	0.82	0.54
GB13	50.35	-3.42	-2.17	-2.13	-1.00	-0.98
GB14	54.20	-0.48	5.02	3.93	1.17	1.50
GB31	52.30	-3.11	-1.71	-1.71	-0.90	-0.90
GB37	53.23	-1.45	-3.10	-3.08	-1.25	-1.25
GB38	50.47	0.10	-4.05	-4.03	-2.20	-2.19
GB44	51.13	-3.20	6.21	6.69	0.61	1.42
GB45	52.17	-0.17	6.28	6.00	3.48	1.94
GB51	52.33	-0.46	12.56	16.60	4.11	4.50
GR01	41.45	42.49	0.50	2.07	0.40	1.05
NL09	53.2	6.16	-3.21	-1.63	-1.18	-0.19
NL10	51.32	5.51	3.48	3.52	0.92	-0.29
NL91	52.18	4.30	11.81	6.42	1.48	-0.81

912
 913

914

915 Table 8: The tropospheric chemical budget for the CH₂O given in Tg CH₂O yr⁻¹ during 2006 for the 1°
 916 x 1° simulation. Percentage differences are shown against the corresponding 3° x 2° simulation.
 917

Budget Term	Global	%	SH	%	Tropics	%	NH	%
CH ₂ O CP	1919	-1.1	147	-0.3	1491	-1.0	281	-2.0
CH ₂ O CD	1739	-1.6	134	-0.5	1349	-1.1	256	-2.3
CH ₂ O Dep.	193	3.1	15	2.0	149	3.9	29	-

918

919 Table 9: The seasonal mean biases of daily [SO₂] (µg m⁻³) at 13:00 for DJF and JJA, when taking the
 920 difference between measurements-model values. Values are shown for both the 3° x 2° and 1° x 1°
 921 simulations. Those with differences < 5% are considered to exhibit no discernible change in the bias.
 922

EMEP Station	Lat	Lon	DJF 3° x 2°	DJF 1° x 1°	JJA 3° x 2°	JJA 1° x 1°
AT02	47.46	16.46	-3.34	-3.15	-0.89	-0.53
AT05	46.40	12.58	-0.42	-0.41	-0.14	-0.14
AT48	47.50	14.26	-0.64	-0.63	-0.14	-0.15
CZ03	49.35	15.50	-3.52	3.65	-0.69	0.64
ES07	37.14	-3.32	1.22	0.73	0.38	0.31
ES08	43.26	-4.51	-2.98	-3.21	-1.19	-1.58
ES09	41.16	-3.80	-0.62	-0.61	-0.42	-0.42
ES10	42.19	3.19	2.37	2.45	1.93	1.53
ES11	38.28	-6.55	-0.63	-0.61	-0.70	-0.70
ES12	39.50	-1.60	-0.47	-0.45	-0.32	-0.32
ES13	41.17	-5.52	-0.81	2.71	-0.78	0.55
ES14	41.24	0.43	-0.70	-0.67	-0.47	-0.47
ES15	39.31	-4.21	-0.40	-0.37	-0.45	-0.46
ES16	43.13	-7.41	-3.84	-3.82	-1.66	-1.66
GB37	52.30	-3.11	-2.92	-2.91	-1.72	-1.72
GB38	53.23	-1.45	2.93	2.75	0.39	1.33
GB43	51.14	-4.42	-1.49	4.77	-2.03	-0.63
GB45	52.17	-0.17	3.87	7.20	1.01	1.77
GR01	38.22	23.50	1.70	2.77	0.74	1.50
NL07	52.50	6.34	2.58	-1.67	0.46	-1.03
NL08	52.70	5.12	1.77	1.56	-0.14	-0.30
NL09	53.2	6.16	2.53	2.16	0.47	0.27

923

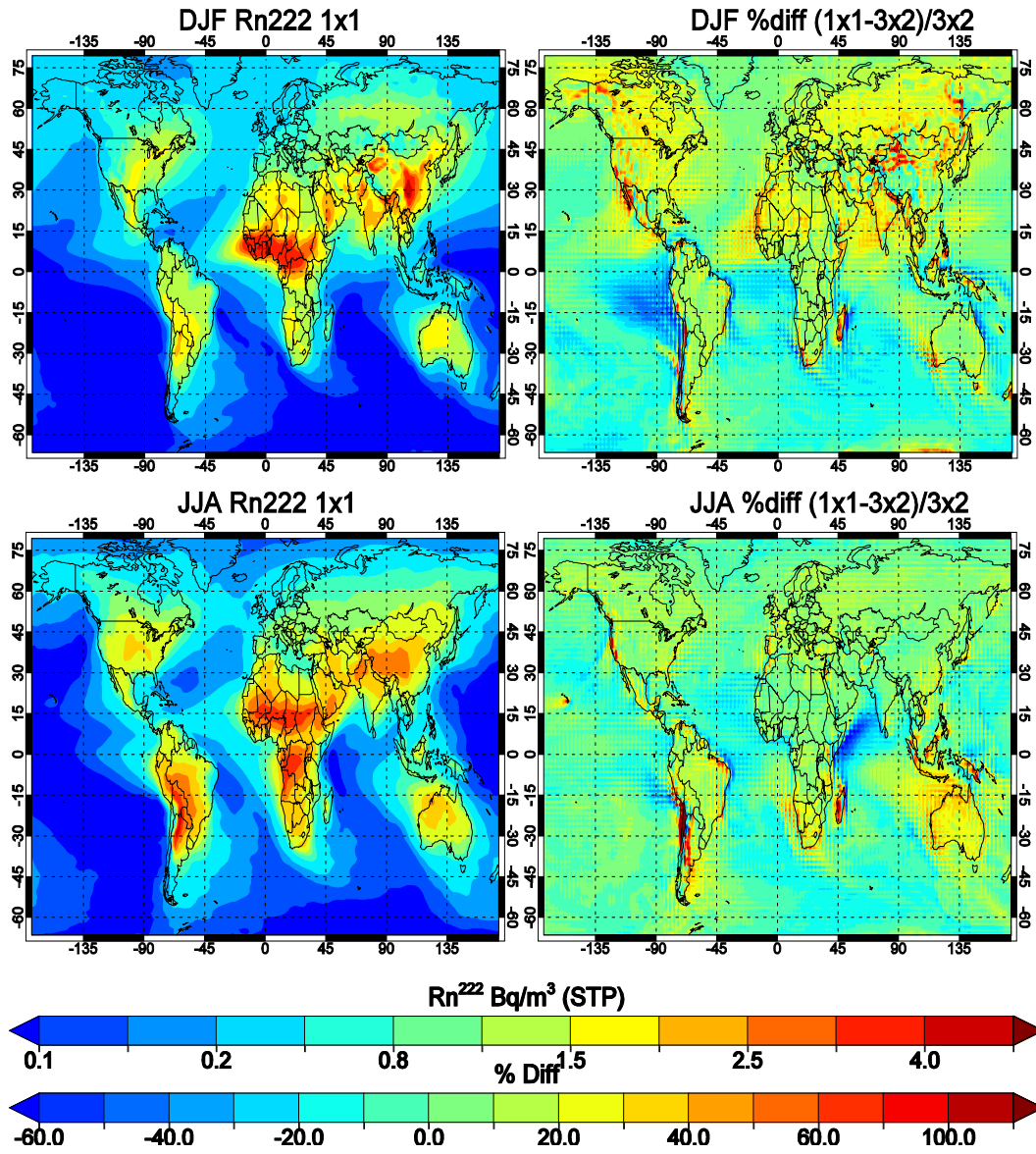


Figure 1: The seasonal distributions of Rn^{222} averaged between 800 and 900hPa for DJF (top) and JJA (bottom) for the $3^\circ \times 2^\circ$ (left) and $1^\circ \times 1^\circ$ (right) simulation, with the associated percentage differences when compared against the $3^\circ \times 2^\circ$ simulation.

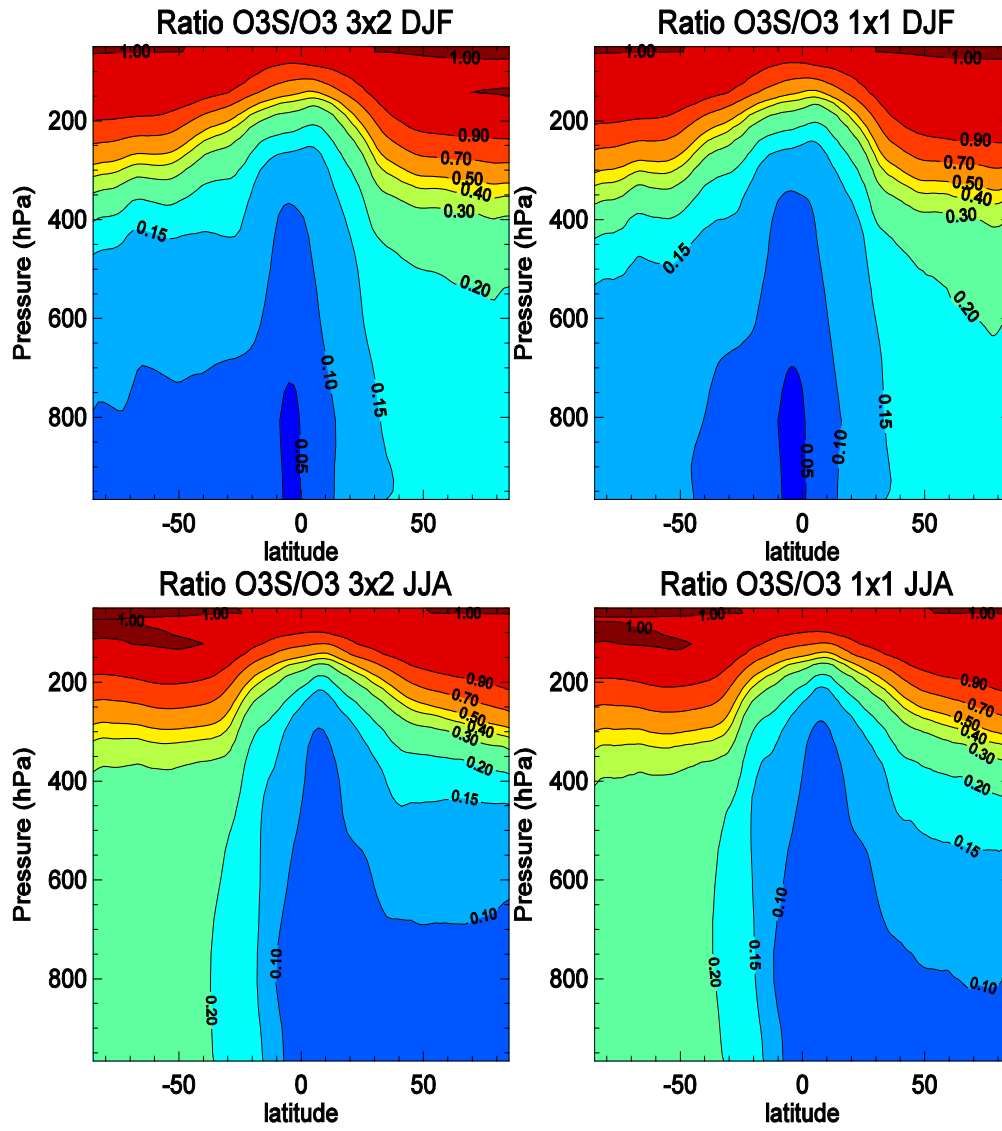


Figure 2: Zonal mean seasonal distribution of the TM5-MP O_3S/O_3 ratio for the $3^\circ \times 2^\circ$ (left) and $1^\circ \times 1^\circ$ (right) simulations.

935

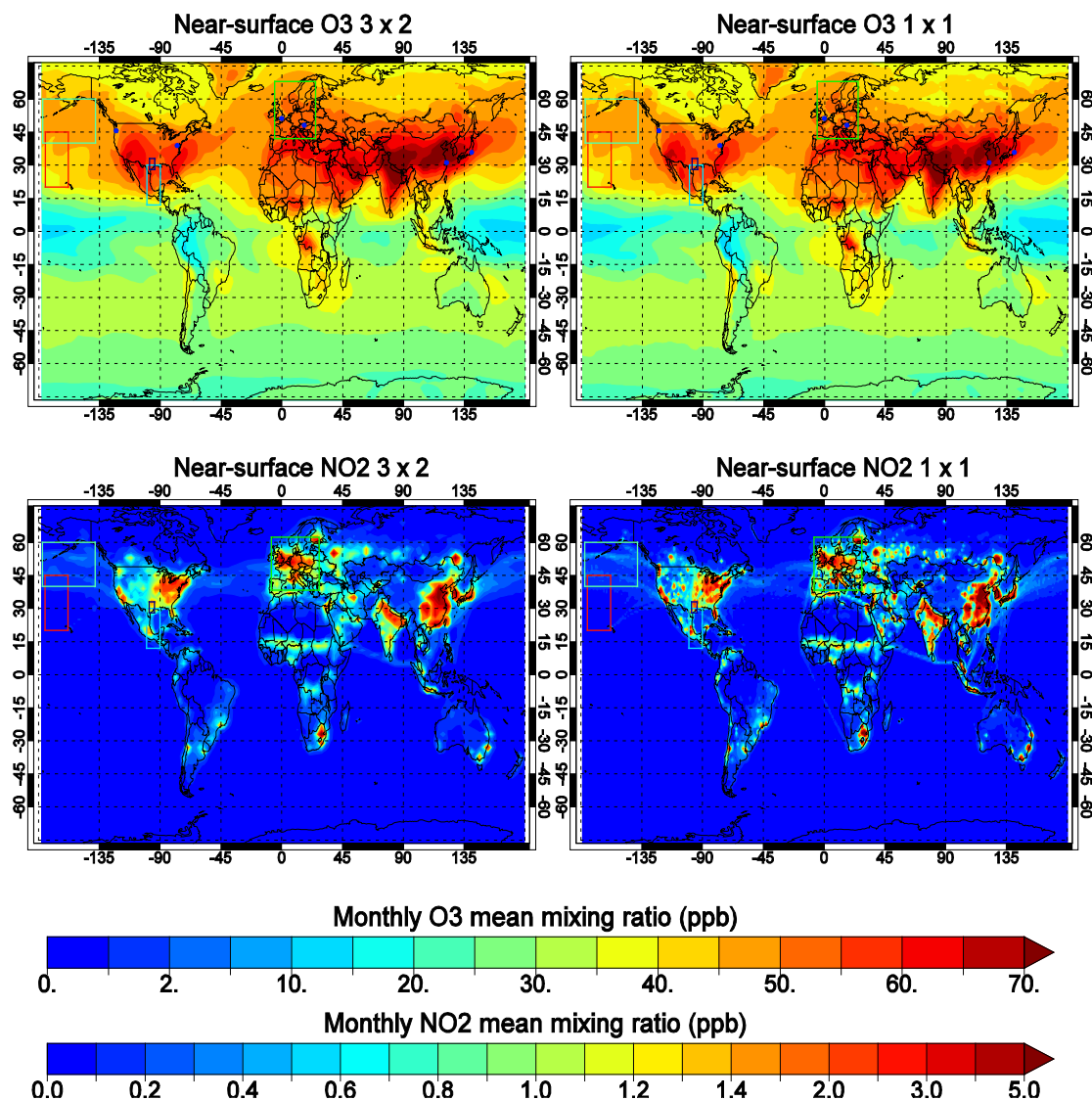
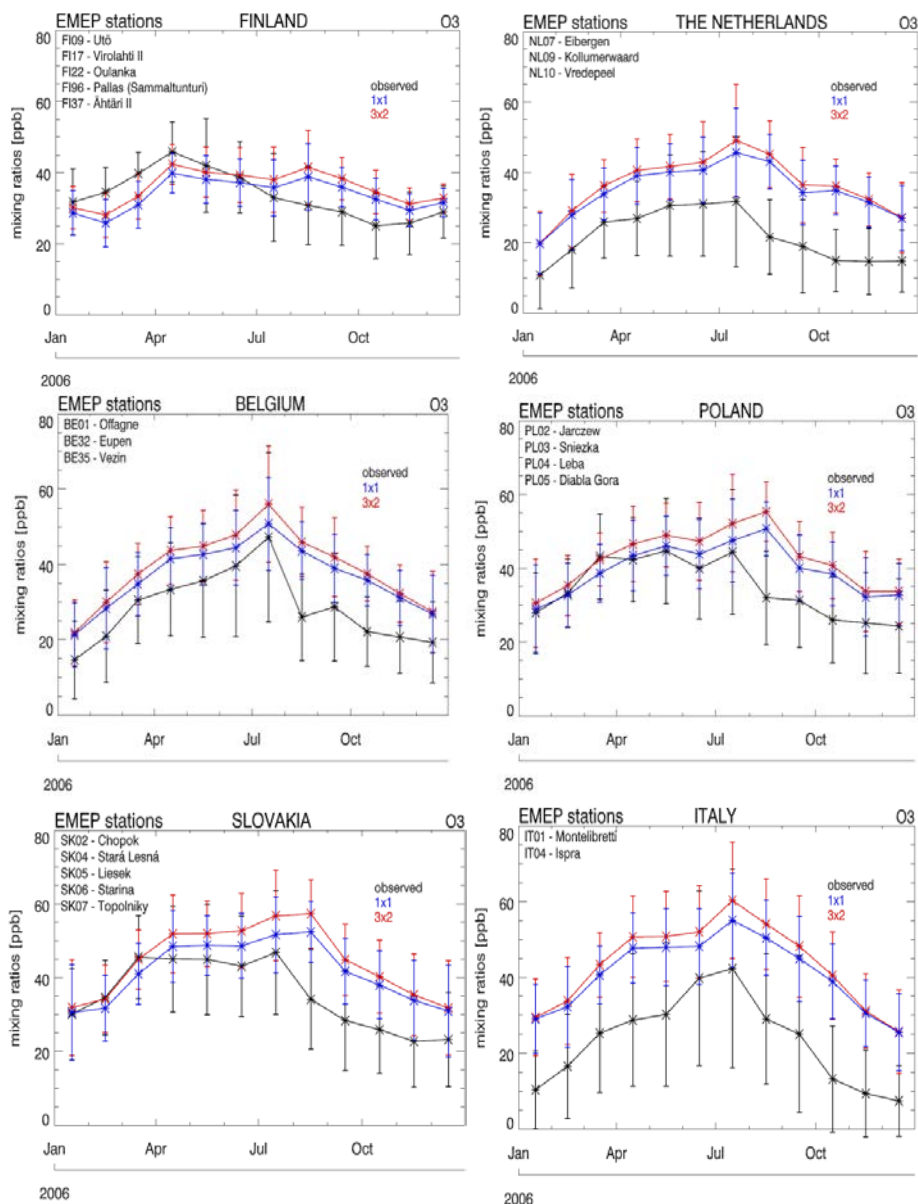


Figure 3: The near-surface distribution in tropospheric O_3 (top) and NO_2 (bottom) for May 2006 from the $3^\circ \times 2^\circ$ (left) and $1^\circ \times 1^\circ$ (right) TM5-MP simulations. The blue points represent the location of the MOZAIC airports used for comparisons. Also shown are the locations of the INTExB and Texas-AQSII measurement campaigns, and the extent of the EMEP network in the European domain, used for the validation of the resulting O_3 and NO_2 distributions.

936
937
938
939
940
941
942
943
944

945



946

947

948

949

950

951

952

953

954

955

956

Figure 4: Comparisons of the seasonal variability in TM5-MP mass mixing ratios for surface O_3 against composites of measurements taken across the EMEP monitoring network for 2006. Both the co-located TM5-MP $3^\circ \times 2^\circ$ and $1^\circ \times 1^\circ$ monthly mean values are shown, along with the $1-\sigma$ variability for Finland, The Netherlands, Belgium, Poland, Slovakia and Italy. Individual stations that are aggregated are given in the panels.

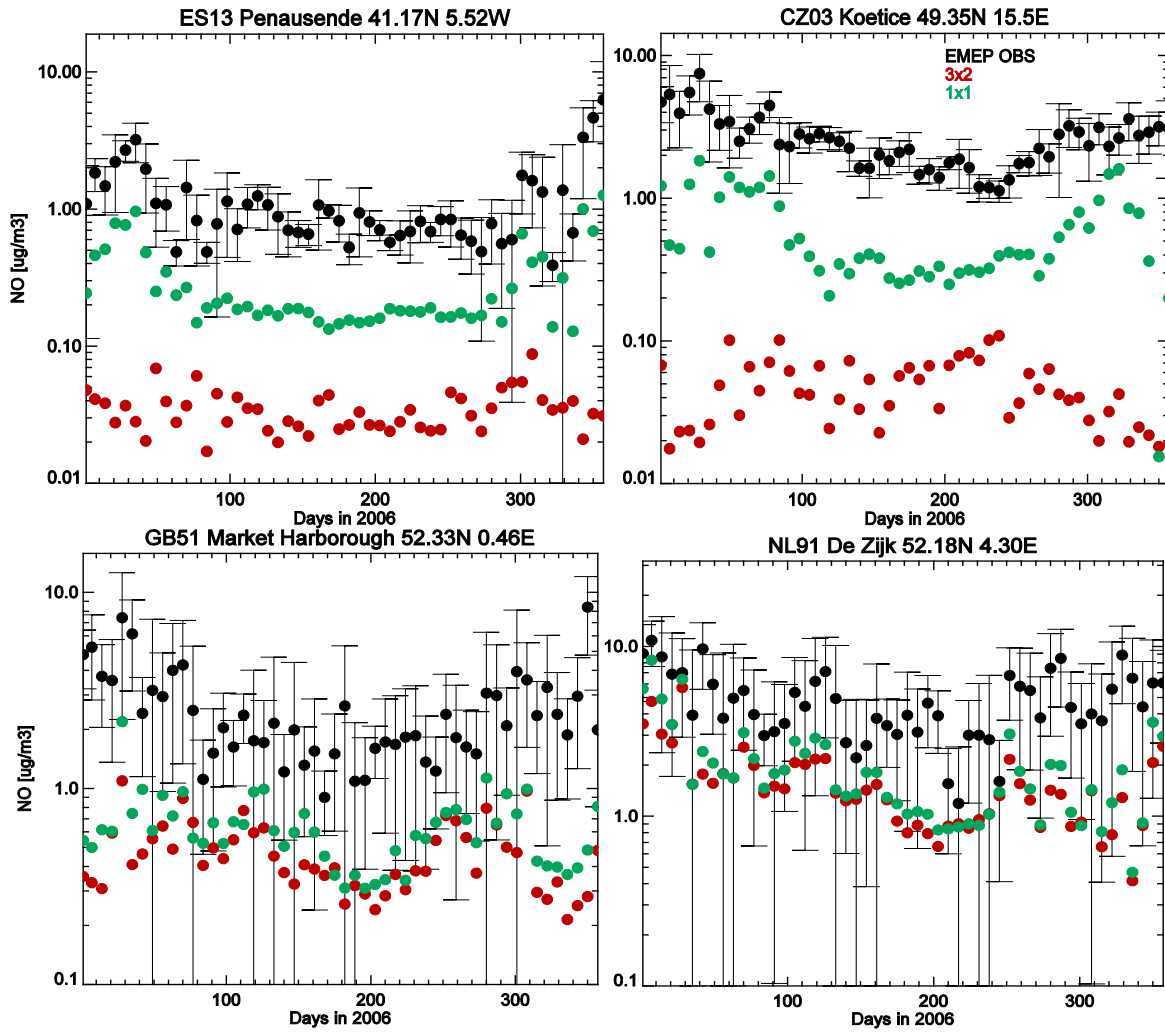


Figure 5: Comparison of TM5-MP weekly [NO] sampled at 13:00 UT each day during 2006 with observed [NO] ($\mu\text{g m}^{-3}$). The selected sites shown are in the Czech Republic (top left), Spain (top right), Great Britain (bottom left) and The Netherlands (bottom right).

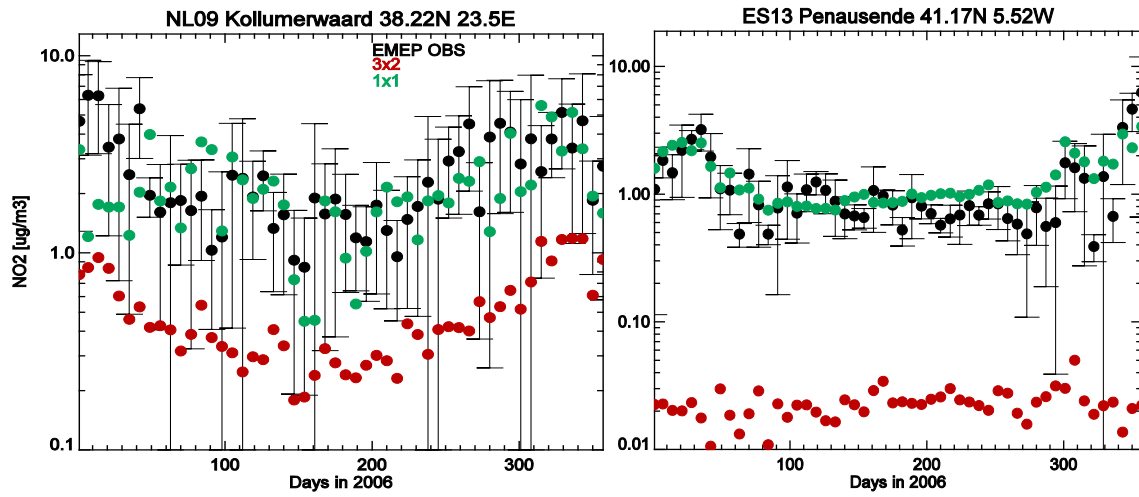


Figure 6: Comparison of weekly TM5-MP [NO₂] sampled at 13:00 UT each day during 2006 with observed [NO₂] ($\mu\text{g m}^{-3}$). The selected sites shown are in The Netherlands (left) and Spain (right).

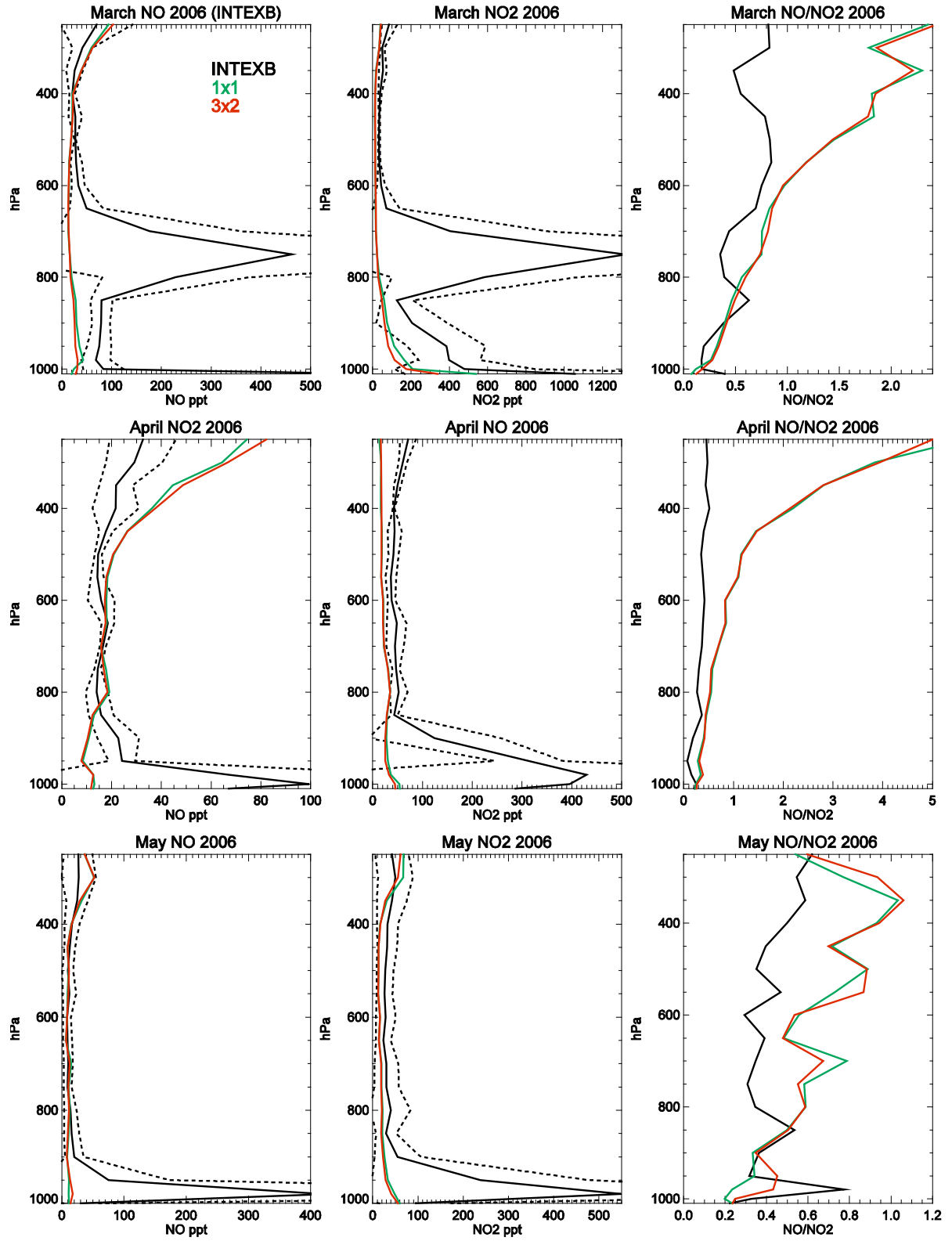


Figure 7: Monthly mean comparisons of NO (left), NO₂ (middle) and the resulting NO/NO₂ ratio (right) from INTEX-B measurements and TM5-MP simulations. The dotted line represents the 1- σ deviation in the mean of the measurements. For details of the locations for each month the reader is referred to Singh et al. (2009).

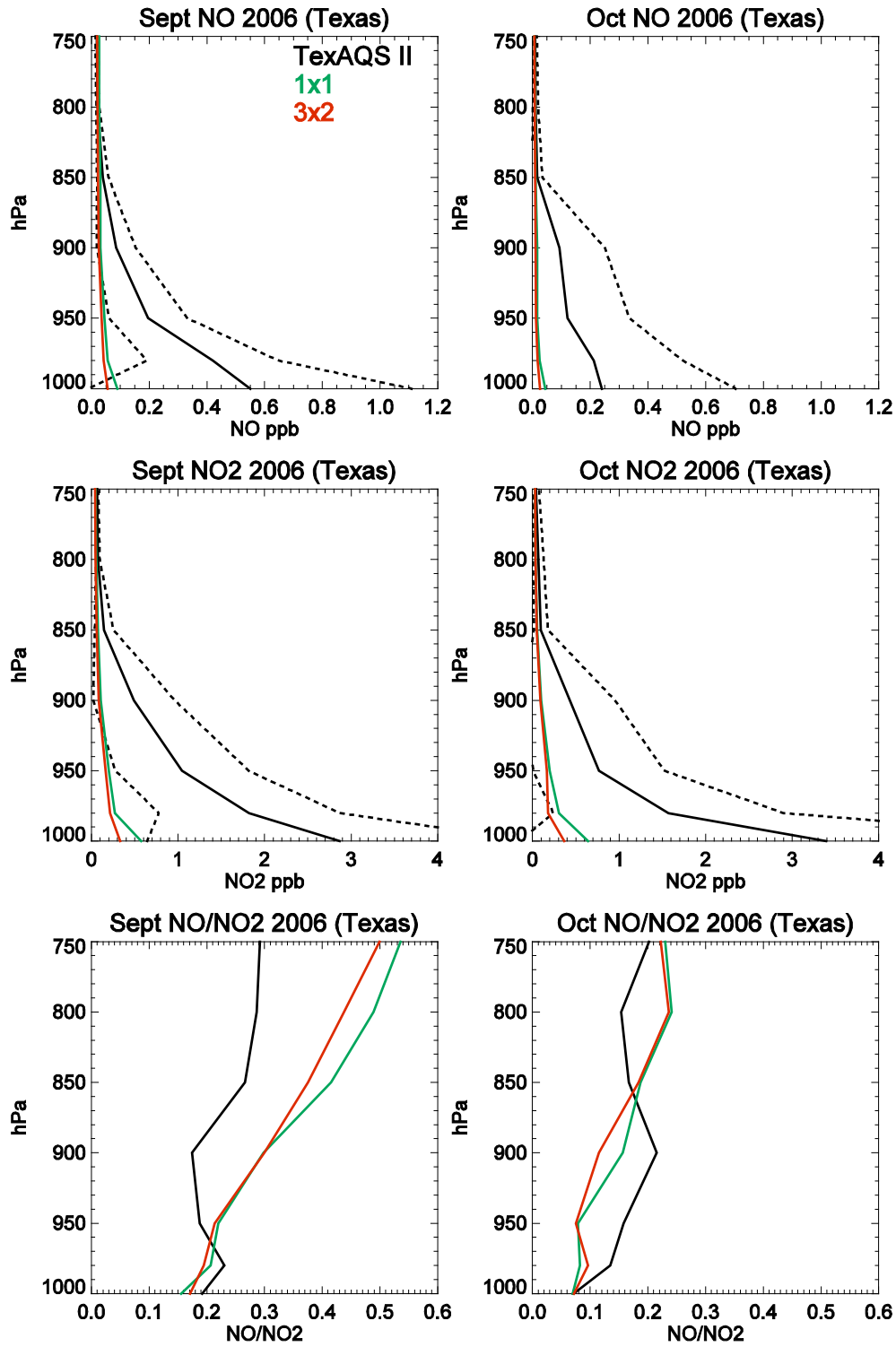


Figure 8: Monthly mean comparisons of NO (left), NO₂ (middle) and the resulting NO/NO₂ ratio (right) from the TexAQSI campaign during September and October 2006 and TM5-MP simulations. The dotted line represents the 1-σ deviation in the mean of the measurements. For details of the locations for each month the reader is referred to Parrish et al. (2009).

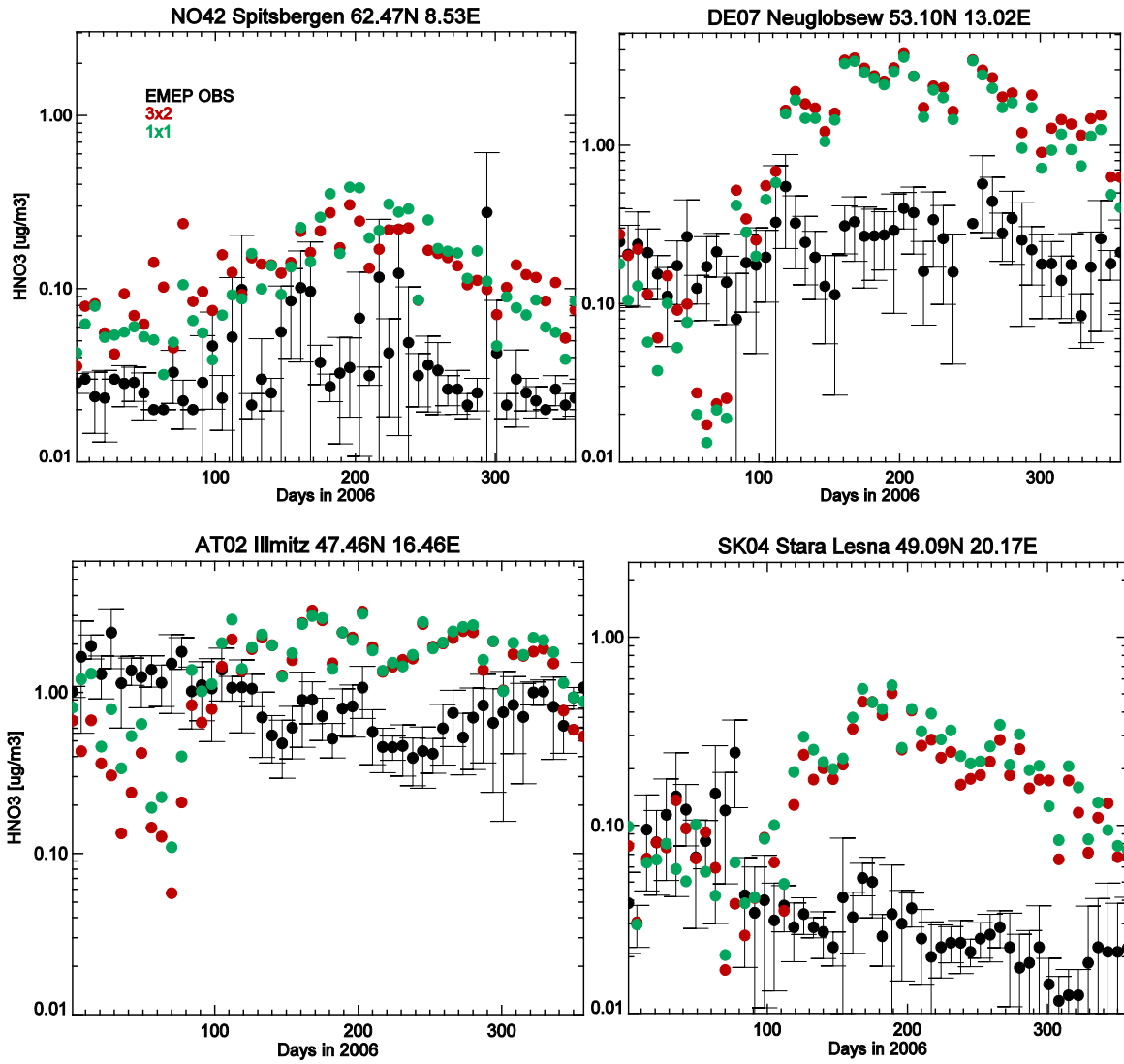


Figure 9: Comparison of weekly $[\text{HNO}_3]$ ($\mu\text{g m}^{-3}$) from both $3^\circ \times 2^\circ$ and $1^\circ \times 1^\circ$ simulations at 4 selected EMEP sites for 2006. The $1\text{-}\sigma$ deviation in the weekly observations are shown as error bars. The selected sites shown are in Norway (top left), Germany (top right), Austria (bottom left) and Slovakia (bottom right).

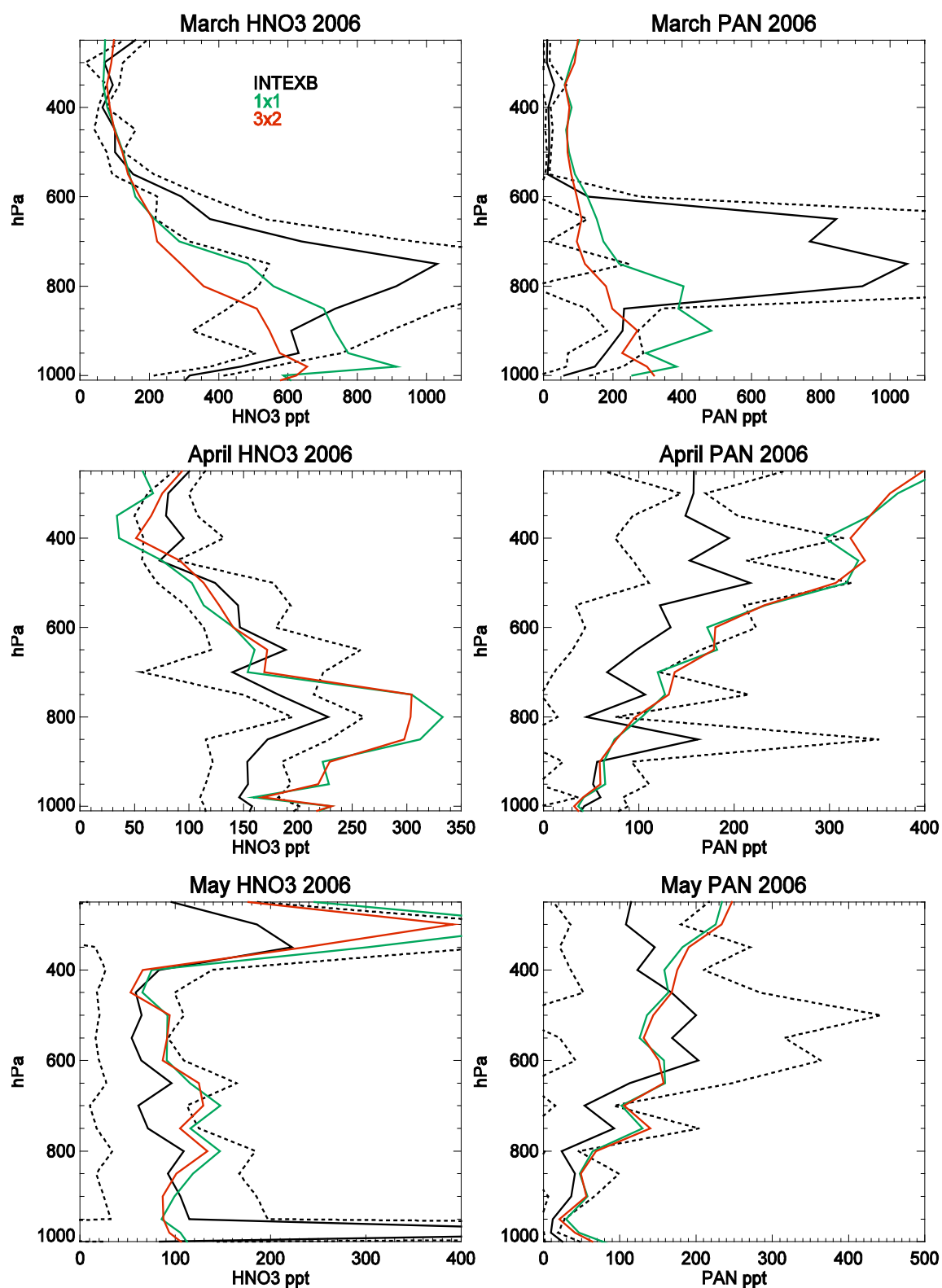


Figure 10: Monthly mean comparisons of HNO₃ (left) and PAN (right) from the INTEX-B measurements and TM5-MP simulations. The dotted line represents the 1-σ deviation in the mean of the measurements. For details of the locations for each month the reader is referred to Singh et al. (2009).

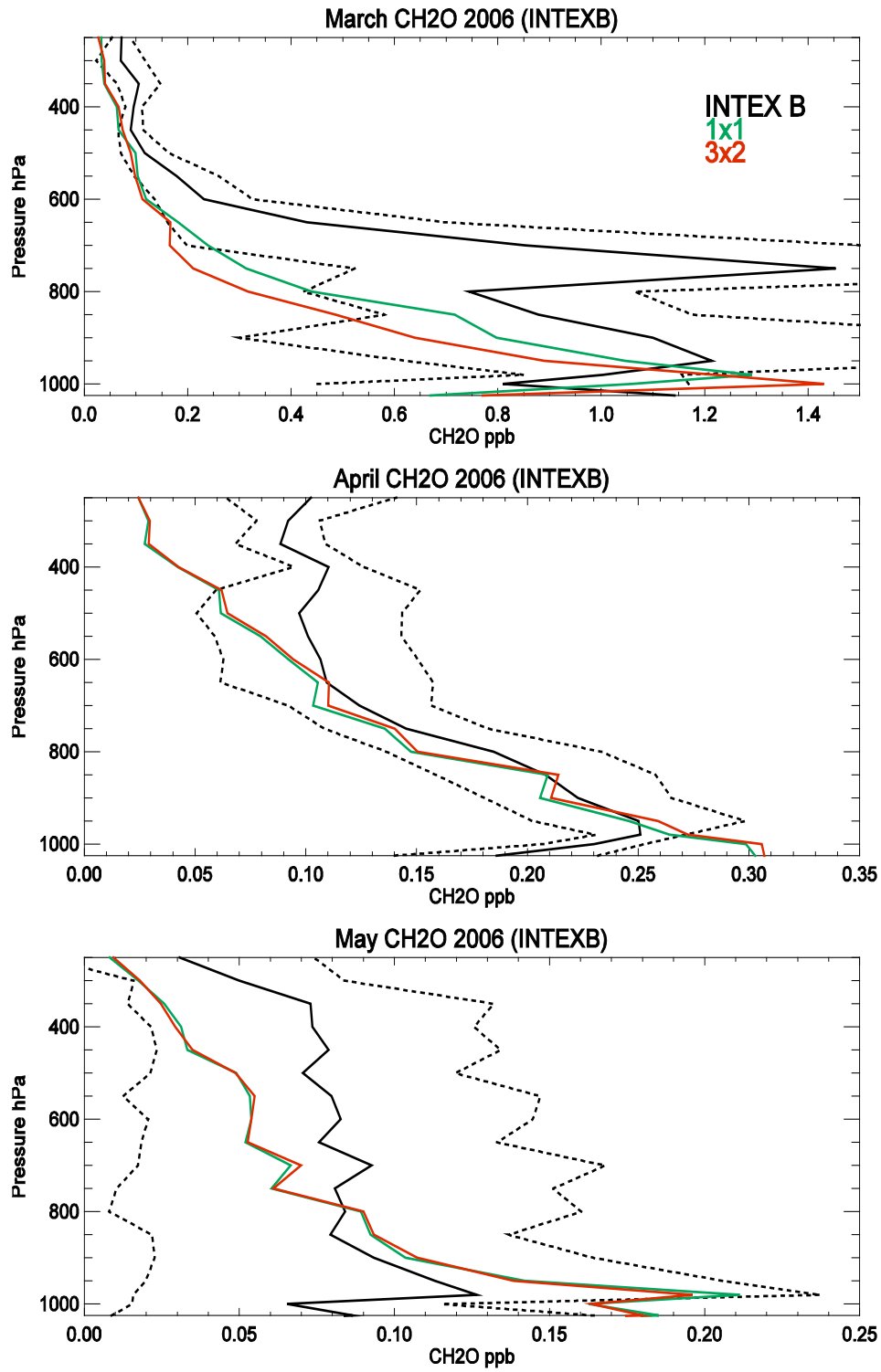


Figure 11: Comparisons of the vertical distribution of CH_2O from both $3^\circ \times 2^\circ$ and $1^\circ \times 1^\circ$ simulations against measurements made as part of the INTEX-B during 2006. The dotted line represents the $1\text{-}\sigma$ deviation in the mean of the measurements. For details on the exact location of the flights the reader is referred to Parrish et al. (2009).

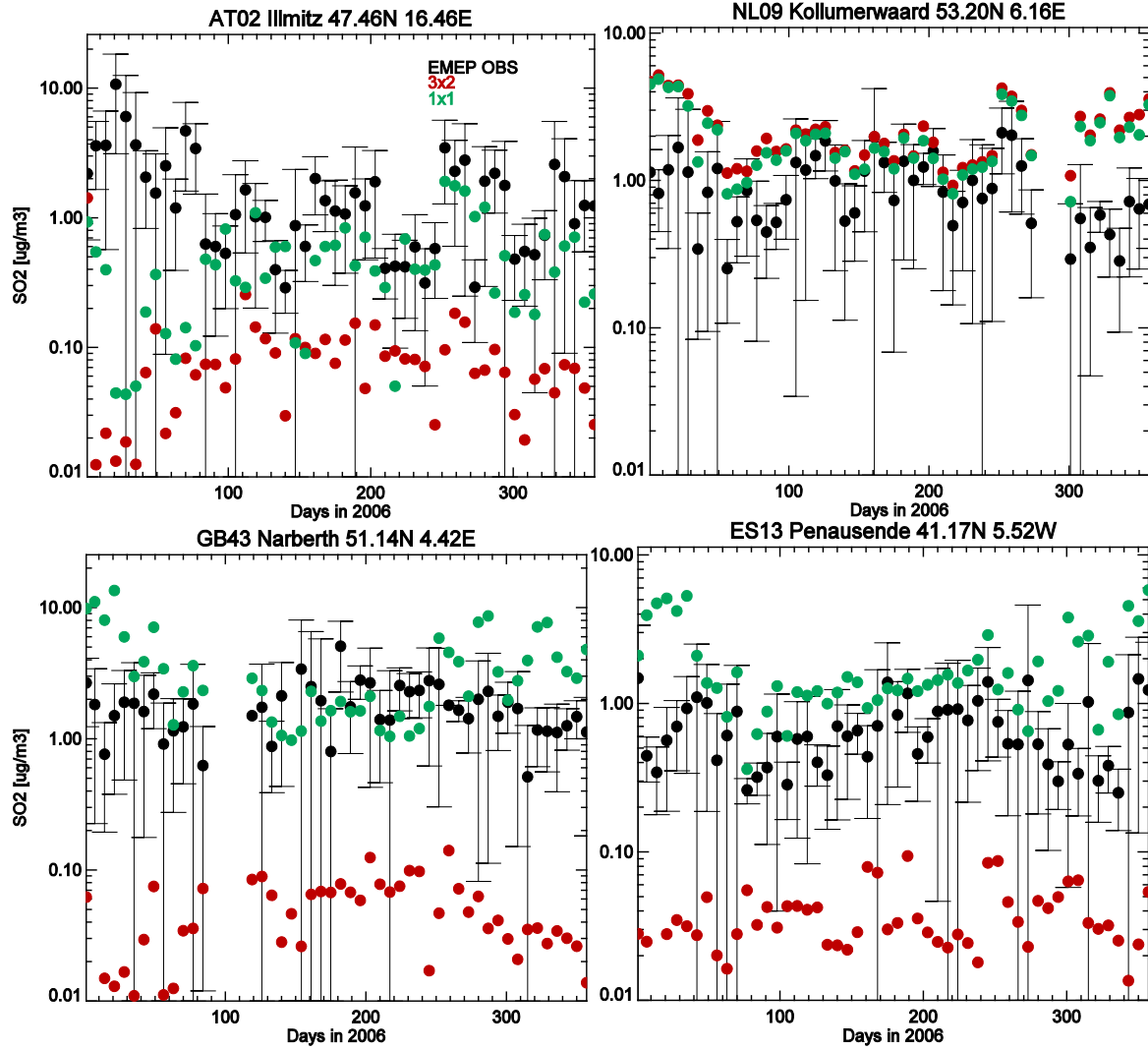


Figure 12: Comparison of weekly $[\text{SO}_2]$ ($\mu\text{g m}^{-3}$) at 13:00 from both the $3^\circ \times 2^\circ$ and $1^\circ \times 1^\circ$ simulations at 4 selected EMEP sites for 2006. The selected sites shown are in Austria (top left), the Netherlands (top right), Great Britain (bottom left) and Spain (bottom right).

1021

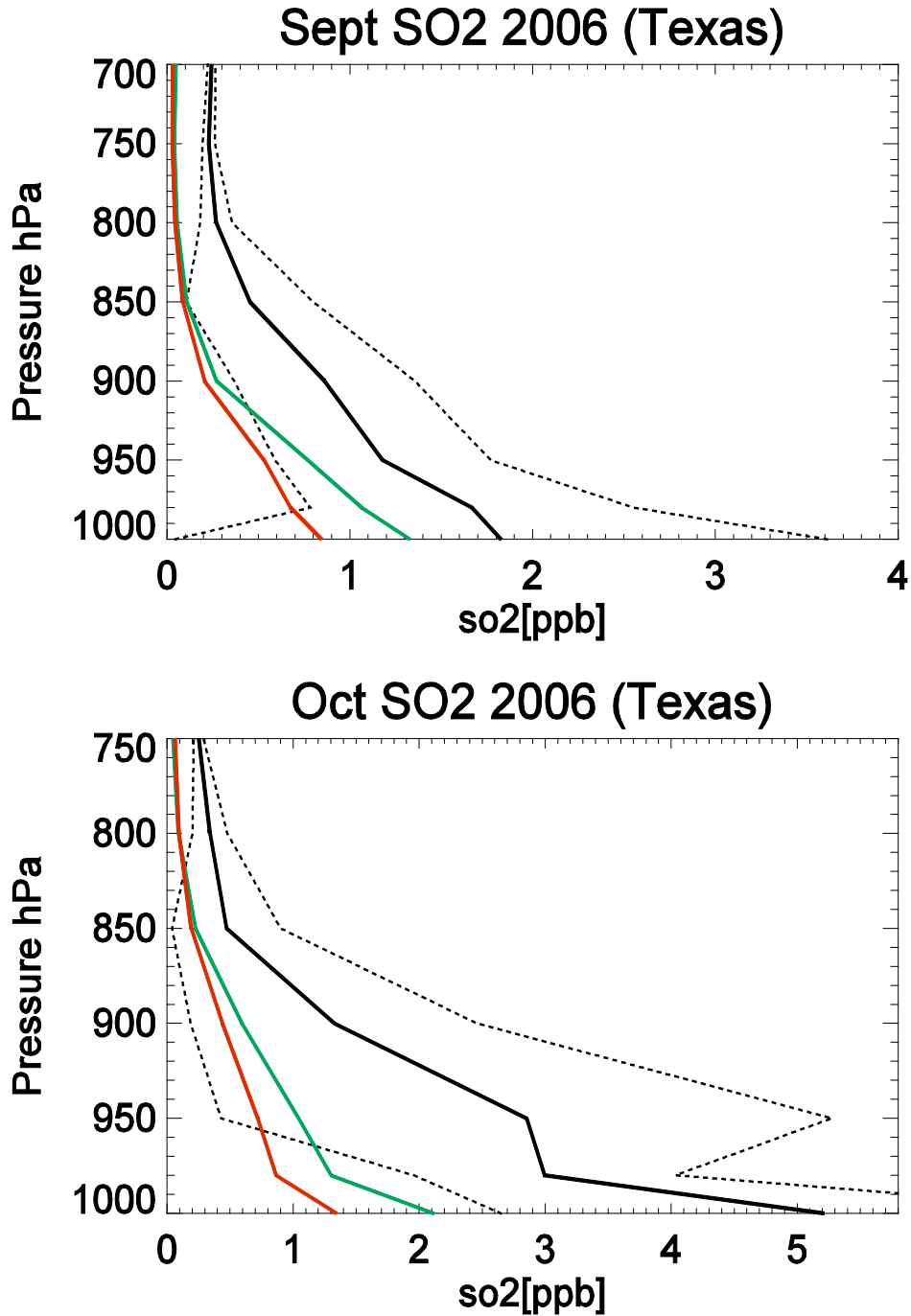


Figure 13: Comparisons of the monthly tropospheric SO₂ profile assembled from data taken during September and October 2006 as part of TexAQS II. The 1- σ deviation of the mean derived from the measurements is shown as the dotted line. For details of the flight paths the reader is referred to Parrish et al. (2009).

1022
1023
1024
1025
1026
1027
1028

References

- Aan de Brugh, J. M. J., Schaap, M., Vignati, E., Dentener, F., Kahnert, M., Sofiev, M., Huijnen, V., and Krol, M. C.: The European aerosol budget in 2006, *Atms. Phys. Chem.*, 11, 1117-1139, doi:10.5194/acp-11-1117-2011, 2011.
- Aas, W., Hjellbrekke, A.-G., Schaug, J., and Solberg, S.: Data quality 1999, quality assurance and field comparisons, Kjeller, Norwegian Institute for Air Research, EMEP/CCC Report 6/2001, 2001.
- Abbatt, J. P. D., Lee, A. K. Y., and Thornton, J. A.: Quantifying trace gas uptake to tropospheric aerosol: recent advances and remaining challenges, *Chem. Soc. Rev.*, 41, 6555–6581, doi:10.1039/c2cs35052a, 2012.
- Alonza Gray, B., Wang, Y., Gu, D., Bandy, A., Mauldin, L., Clarke, A., Alexander, B., and Davis, D. D.: Sources, transport, and sinks of SO₂ over the equatorial Pacific during the Pacific Atmospheric Sulfur Experiment, *J. Atmos. Chem.*, 68, 27-53, doi: 10.1007/s10874-010-9177-7, 2011.
- Atkinson, R., Baulch, D. L., Cox, R. A., Crowley, J. N., Hampson, R. F., Hynes, R. G., Jenkin, M. E., Rossi, M. J., and Tore, J., Evaluated kinetic and photochemical data for atmospheric chemistry: Volume I –gas phase reactions of O_x, HO_x, NO_x and SO_x species, *Atmos. Chem. Phys.*, 4, 1461-1738, 2004.
- Atkinson, R., Baulch, D. L., Cox, R. A., Crowley, J. N., Hampson, R. F., Hynes, R. G., Jenkin, M. E., Rossi, M. J., and Tore, J., Evaluated kinetic and photochemical data for atmospheric chemistry: Volume II –gas phase reactions of organic species, *Atmos. Chem. Phys.*, 6, 3625-4055, 2006.
- Bândă, N., Krol, M., van Noije, T., van Weele, M., Williams J. E., Le Sager, P., Niemeier, U., Thomason, L. and Röckmann, T.: The effect of stratospheric sulfur from Mount Pinatubo on tropospheric oxidizing capacity and methane, *J. Geophys. Res. Atmos.*, 120, doi:10.1002/2014JDO22137, 2015.
- Boersma, K. F., Jacob, D. J., Eskes, H. J., Pinder, R. W., Wang, J. and van der A, R. J.: Intercomparison of SCIAMACHY and OMI tropospheric NO₂ columns: observing the diurnal evolution of chemistry and emissions from space, *J. Geophys. Res.*, 2, 113, 1-14, doi:10.1029/2007JD008816, 2008.
- Boersma, K. F., Eskes, H. J., Dirksen, R. J., van der A, R. J., Veefkind, J. P., Stammes, P., Huijnen, V., Kleipool, Q. L., Sneep, M., Claas, J., Leitao, J., Richter, A., Zhou, Y. and Brunner, D.: An improved tropospheric NO₂ column retrieval algorithm for the Ozone Monitoring Instrument, *Atmos. Meas. Tech.*, 4, 1905-1928, 2011.
- Bönisch, H., Hoor, P., Gurk, Ch., Feng, W., Chipperfield, M., Engel, A., and Bregman, B.: Model evaluation of CO₂ and SF₆ in the extratropical UT/LS region, *J. Geophys. Res.*, 113, D06101, doi:10.1029/2007JD008829, 2008.
- Bregman, B., Segers, A., Krol, M., Meijer, E., and van Velthoven, P.: On the use of mass-conserving wind fields in chemistry-transport models, *Atmos. Chem. Phys.*, 3, 447–457, doi:10.5194/acp-3-447-2003, 2003.
- Browne, E. C., Perring, A. E., Wooldridge, P. J., Apel, E., Hall, S. R., Huey, L. G., Mao, J., Spencer, K. M., St. Clair, J. M., Weinheimer, A. J., Wisthaler, A., and Cohen, R. C.: Global and regional effects of the photochemistry of CH₃ONO₂: evidence from ARCTAS, *Atmos. Chem. Phys.*, 11, 4209-4219, 2011.

- 1064 Carslaw, D. C. and Beevers, S. D.: Estimations of road vehicle primary NO₂ exhaust emission fractions using
1065 monitoring data in London, *Atmos. Environ.*, 39(1), 167-177, 2005.
- 1066 De Smedt, I., Muller, J.-F., Stavrou, T., van der A., R., Eskes, H. and Van Roozendael, M.: Twelve years of
1067 global observations of formaldehyde in the troposphere using GOME and SCIAMACHY sensors, *Atmos.*
1068 *Chem. Phys.*, 8, 4947-4963, 2008.
- 1069 Dee, D. P., Uppala, S. M., Simmons, A. J., Berrisford, P., Poli, P., Kobayashi, S., Andrae, U., Balmaseda, M.
1070 A., Balsamo, G., Bauer, P., Bechtold, P., Beljaars, A. C. M., van de Berg, L., Bidlot, J., Bormann, N., Delsol,
1071 C., Dragani, R., Fuentes, M., Geer, A. J., Haimberger, L., Healy, S. B., Hersbach, H., Hólm, E. V., Isaksen, I.,
1072 Kållberg, P., Köhler, M., Matricardi, M., McNally, A. P., Monge-Sanz, B. M., Morcrette, J.-J., Park, B.-K.,
1073 Peubey, C., de Rosnay, P., Tavolato, C., Thépaut, J.-N. and Vitart, F.: The ERA-Interim reanalysis:
1074 configuration and performance of the data assimilation system, *Q. J. Royal Met. Soc.*, 137, 656, 553-597, 2011.
- 1075 Dunlea, E. J., Herndon, S. C., Nelson, D. D., Volkamer, R. M., San Martini, F., Sheehy, P. M., Zahniser,
1076 M. S., Shorter, J. H., Wormhoudt, J. C., Lamb, B. K., Allwine, E. J., Gaffney, J. S., Marley, N. A., Grutter, M.,
1077 Marquez, C., Blanco, S., Cardenas, B., Retama, A., Ramos Villegas, C. R., Kolb, C. E., Molina, L. T., and
1078 Molina, M. J.: Evaluation of nitrogen dioxide chemiluminescence monitors in a polluted urban environment,
1079 *Atmos. Chem. Phys.*, 7, 2691–2704, 2007, <http://www.atmos-chem-phys.net/7/2691/2007/>
- 1080 Dupuy, E., Urban, J., Ricaud, P., Le Flochmoën, E., Latié, N., Murtagh, D., De La Noë, J., El Amraoui, L.,
1081 Eriksson, P., Forkman, P., Frisk, U., Jégou, F., Jiménez, C. and Olberg, M.: Strato-mesospheric measurements
1082 of carbon monoxide with the Odin Sub-Millimetre Radiometer: Retrieval and first results, *Geophys. Res.*
1083 *Letts.*, 31, L20101, doi:10.1029/2004GL020558, 2004.
- 1084 Emmons, L. K., Walters, S., Hess, P. G., Lamarque, J.-F., Pfister, G. G., Fillmore, D., Granier, C., Guenther,
1085 A., Kinnison, D., Laepple, T., Orlando, J., Tie, X., Tyndall, G., Wiedinmyer, C., Baughcum, S. L., and Kloster,
1086 S.: Description and evaluation of the Model for Ozone and Related chemical Tracers, version 4 (MOZART-4),
1087 *Geosci. Model Dev.*, 3, 43–67, doi: 10.5194/gmd-3-43-2010, 2010.
- 1088 Evans, M. J. and Jacob, D. J.: Impact of new laboratory studies of N₂O₅ hydrolysis on global model budgets of
1089 tropospheric nitrogen oxides, ozone and OH, *Geophys. Res. Letts.*, 32, doi:10.1029/2005GL022469, 2005.
- 1090 Fortuin, J. P. F. and Kelder, H.: An ozone climatology based on ozonesonde and satellite measurements. *J.*
1091 *Geophys. Res.*, 103, 31709–31734, 1998.
- 1092 Ganzeveld, L., Helmig, D., Fairall, C. W., Hare, J. and Pozzer, A.: Atmosphere-ocean ozone exchange: A
1093 global modeling study of biogeochemical, atmospheric, and waterside turbulence dependencies, *Global*
1094 *Biogeo. Cycles*, 23, GB4021, doi:10.1029/2008GB003301, 2009.
- 1095 Gonçalves, M., Dabdub, D., Chang, W. L., Jorba, O. and Baldasano, J. M.: Impact of HONO sources on the
1096 performance of mesoscale air quality models, *Atmos. Environ.*, 54, Pages 168–176,
1097 doi:10.1016/j.atmosenv.2012.02.079, 2012.
- 1098 Gonzi, S., Palmer, P. I., Barkley, M., De Smedt, I. and Roozendael, M. V.: Biomass burning emission
1099 estimates inferred from satellite column measurements of HCHO: Sensitivity to co-emitted aerosol and
1100 injection height, *Geophys. Res. Letts.*, 38, L14807, 2011.

- 1101 Granier, C., Bessagnet, B., Bond, T., D'Angiola, A., Denier van der Gon, H., Frost, G. J., Heil, A., Kaiser, J.
 1102 W., Kinne, S., Klimont, Z., Kloster, S.-F., Lamarque, J., Lioussé, C., Masui, T., Meleux, F., Mieville, A.,
 1103 Ohara, T., Raut, J.-C., Riahi, K., Schultz, M. G., Smith, S. J., Thompson, A., van Aardenne, J., van der Werf,
 1104 G. R., and van Vuuren, D. P.: Evolution of anthropogenic and biomass burning emissions of air pollutants at
 1105 global and regional scales during the 1980–2010 period, *Climate Change*, 109, 163–190, doi: 10.1007/s10584-
 1106 011-0154-115, 2011.
- 1107 GroöB, J.-U. and Russell III, J. M.: Technical note: A stratospheric climatology for O₃, H₂O, CH₄, NO_x, HCl
 1108 and HF derived from HALOE measurements, *Atmos. Chem. Phys.*, 5, 2797–2807, doi:10.5194/acp-5-2797-
 1109 2005, 2005.
- 1110 Halmer M. M., Schmincke H.-U. and Graf H.-F.: The annual volcanic gas input into the atmosphere, in
 1111 particular into the stratosphere: a global data set for the past 100 years, *Journal of Volcanology and*
 1112 *Geothermal Research*, 115, pp. 511–528, 2002.
- 1113 Hardacre, C., Wild, O. and Emberson, L.: An evaluation of ozone dry deposition in global scale chemistry
 1114 climate models, *Atms. Chem. Phys.*, 15, 6419–6436, doi:10.5194/acp-15-6419-2015, 2015.
- 1115 Hauglustaine, D. A., Balkanski, Y. and Schulz, M.: A global model simulation of present and future nitrate
 1116 aerosols and their direct radiative forcing of climate, *Atms. Chem. Phys.*, 14, 11031–11063, doi:10.5194/acp-
 1117 14-11031-2014, 2014.
- 1118 Heckel, A., Kim, S.-W., Frost, G. J., Richter, A., Trainer, M. and Burrows, J. P.: Influence of low spatial
 1119 resolution a priori data on tropospheric NO₂ satellite retrievals, *Atmos. Meas. Tech.*, 4, 1805–1820,
 1120 doi:10.5194/amt-4-1805-2011, 2011.
- 1121 Huijnen, V., Williams, J., van Weele, M., van Noije, T., Krol, M., Dentener, F., Segers, A., Houweling, S.,
 1122 Peters, W., de Laat, J., Boersma, F., Bergamaschi, P., van Velthoven, P., Le Sager, P., Eskes, H., Alkemade,
 1123 F., Scheele, R., Nédelec, P., and Pätz, H.-W., The global chemistry transport model TM5: description and
 1124 evaluation of the tropospheric chemistry version 3.0, *Geosci. Model Dev.*, 3, 445–473, 2010.
- 1125 Holtslag, A. A. and Boville, B. A.: Local versus non-local boundary layer diffusion in a global climate model,
 1126 *J. Climate*, 10, 1825–1842, 1993.
- 1127 Huijnen, V., Williams, J. E., and Flemming, J.: Modeling global impacts of heterogeneous loss of HO₂ on
 1128 cloud droplets, ice particles and aerosols, *Atmos. Chem. Phys. Discuss.*, 14, 8575–8632, doi: 10.5194/acpd-14-
 1129 8575-2014, 2014.
- 1130 Jacob, D. J., Prather, M. J., Rasch, P. J., Shia, R. L., Balkanski, Y. J., Beagley, S. R., Bergmann, D. J.,
 1131 Blackshear, W. T., Brown, M., Chiba, M., Chipperfield, M. P., de Grandpré, J., Dignon, J. E., Feichter, J.,
 1132 Genthon, C., W. L. Grose, W. L., Kasibhatla, P. S., Köhler, I., Kritz, M. A., Law, K., Penner, J. E., Ramonet,
 1133 M., Reeves, C. E., Rotman, D. A., Stockwell, D. Z., Van Velthoven, P. F. J., Verver, G., Wild, O., Yang, H and
 1134 Zimmermann, P.: Evaluation and intercomparison of global atmospheric transport models using ²²²Rn and
 1135 other short-lived tracers, *J. Geophys. Res.*, 102(D5), 5953–5970, doi:10.1029/96JD02955, 1997.
- 1136 Jacob, J. D.: Heterogeneous chemistry and tropospheric ozone, *Atmos. Environ.*, 34, 2131–2159, 2000.

- 1137 Jégou, F., Urban, J., de La Noë, J., Ricaud, P., Le Flochmoën, E., Murtagh, D. P., Eriksson, P., Jones, A.,
 1138 Petelina, S., Llewellyn, E. J., Lloyd, N. D., Haley, C., Lumpe, J., Randall, C., Bevilacqua, R. M., Catoire, V.,
 1139 Huret, N., Berthet, G., Renard, J. B., Strong, K., Davies, J., Mc Elroy, C. T., Goutail, F., and Pommereau, J. P.:
 1140 Technical Note: Validation of Odin/SMR limb observations of ozone, comparisons with OSIRIS, POAM III,
 1141 ground-based and balloon-borne instruments, *Atmos. Chem. Phys.*, 8, 3385–3409, doi:10.5194/acp-8-3385-
 1142 2008, 2008.
- 1143 Kim, S.-W., McKeen, S. A., Frost, G. J., S.-H. Lee, S.-H., M. Trainer, M., Richter, A., Angevine, W. M.,
 1144 Atlas, E., Bianco, L., Boersma, K. F., Brioude, J., Burrows, J. P., de Gouw, J., Fried, A., Gleason, J., Hilboll,
 1145 A., Mellqvist, J., Peischl, J., Richter, D., Rivera, C., Ryerson, T., te Lintel Hekkert, S., Walega, J., Warneke,
 1146 C., Weibring, P., and Williams, E.: Evaluations of NO_x and highly reactive VOC emission inventories in Texas
 1147 and their implications for ozone plume simulations during the Texas Air Quality Study 2006, *Atmos. Chem.*
 1148 *Phys.*, 11, 11361–11386, doi:10.5194/acp-11-11361-2011, 2011.
- 1149 Koffi, E. N., Bergamaschi, P., Karstens, U., Krol, M., Segers, A., Schmidt, M., Levin, I., Vermeulen, A. T.,
 1150 Fisher, R. E., Kazan, V., Klein Baltink, H., Lowry, D., Manca, G., Meijer, H. A. J., Moncrieff, J., Pal, S.,
 1151 Ramonet, M., Scheeren, H. A., and Williams, A. G.: Evaluation of the boundary layer dynamics of the TM5
 1152 model over Europe, *Geosci. Model Dev.*, 9, 3137–3160, doi:10.5194/gmd-9-3137-2016, 2016.
- 1153 Krol, M., Houweling, S., Bregman, B., van den Broek, M., Segers, A., van Velthoven, P., Peters, W., Dentener,
 1154 F., and Bergamaschi, P.: The two-way nested global chemistry-transport zoom model TM5: algorithm and
 1155 applications, *Atmos. Chem. Phys.*, 5, 417–432, doi:10.5194/acp-5-417-2005, 2005.
- 1156 Lawrence, M. G. and Crutzen, P. J.: The impact of cloud particle gravitational settling on soluble trace gas
 1157 distributions, *Tellus*, 50B, 263–289, 1998.
- 1158 Lee, C., Martin, R. V., van Donkelaar, A., Lee, H., Dickerson, R. R., Hains, J. C., Krotkov, N., Richter, A.,
 1159 Vinnikov, K. and Schwab, J. J.: SO₂ emissions and lifetimes: Estimates from inverse modeling using in situ
 1160 and global, space-based (SCIAMACHY and OMI) observations, *J. Geophys. Res.*, 116, D06304,
 1161 doi:10.1029/2010JD014758, 2011.
- 1162 Lelieveld, J., Peters, W., Dentener, F. J., and Krol, M. C.: Stability of tropospheric hydroxyl chemistry, *J.*
 1163 *Geophys. Res.*, 107(D23), 4715, doi:10.1029/2002JD002272, 2002.
- 1164 Lin, J. T., Martin, R. V., Boersma, K. F., Sneep, M., Stammes, P., Spurr, R., Wang, P., Van Roozendaal, M.,
 1165 Clémer, K., and Irie, H.: Retrieving tropospheric nitrogen dioxide from the Ozone Monitoring Instrument:
 1166 effects of aerosols, surface reflectance anisotropy, and vertical profile of nitrogen dioxide, *Atmos. Chem.*
 1167 *Phys.*, 14, 1441–1461, doi:10.5194/acp-14-1441-2014, 2014.
- 1168 Lee, C., Martin, R. V., van Donkelaar, A., Lee, H., Dickerson, R. R., Hains, J. C., Krotkov, N., Richter, A.,
 1169 Vinnikov, K. and Schwab, J. J.: SO₂ emissions and lifetimes: Estimates from inverse modeling using in situ
 1170 and global, space-based (SCIAMACHY and OMI) observations, *J. Geophys. Res.*, 116, D06304,
 1171 doi:10.1029/2010JD014758, 2011.
- 1172 Louis, J. F.: A parametric model of vertical eddy fluxes in the atmosphere, *Bound.-Layer Meteor.*, 17, 187–
 1173 202, 1979.

- 1174 Marais, E. A., Jacob, D. J., Kurosu, T. P., Chance, K., Murphy, J. C., Reeves, C., Mills, G., Casadio, S., D. B.
 1175 Millet, D. B., Barkley, M. P., Paulot, F., and Mao, J.: Isoprene emissions in Africa inferred from OMI
 1176 observations of formaldehyde columns, *Atms. Chem. Phys.*, 12, 6219–6235, doi:10.5194/acp-12p6219-2012,
 1177 2012.
- 1178 Martin, G. M., Johnson, D. W., and Spice, A.: The measurement and parameterization of effective radius of
 1179 droplets in warm stratocumulus clouds, *J. Atmos. Sci.*, 51, 1823–1842, 1994.
- 1180 Meijer, E. W., van Velthoven, P. F. J., Brunner, D. W., Huntrieser, H., and Kelder, H.: Improvement and
 1181 evaluation of the parameterisation of nitrogen oxide production by lightning, *Phys. Chem. Earth*, 26, 557–583,
 1182 2001.
- 1183 Meloen, J., Siegmund, P., van Velthoven, P., Kelder, H., Sprenger, M., Wernli, H., Kentarchos, A., Roelofs,
 1184 G., Feichter, J., Land, C., Forster, C., James, P., Stohl, A., Collins, W., and Cristofanelli, P.: Stratosphere-
 1185 troposphere exchange: A model and method intercomparison, *J. Geophys. Res.*, 108(D12), 8256,
 1186 doi:10.29/2002JD002274, 2002.
- 1187 Möllner, A. K., Valluvadasan, S., Feng, L., Sprague, M. K., Okumura, M., Milligan, D. B., Bloss, W.J., Sander,
 1188 S. P., Martien, P. T., Harley, R. A., McCoy, A. B. and Carter, W. P. L.: Rate of Gas Phase Association of
 1189 Hydroxyl Radical and Nitrogen Dioxide, *Science*, 330, 646–649, DOI: 10.1126/science.1193030, 2010.
- 1190 Olsen, S. C., McLinden, C. A., and Prather, M. J.: Stratospheric N_2O - NO_y system: Testing uncertainties in a
 1191 three-dimensional framework, *J. Geophys. Res.*, 106, 28771–28784, 2001.
- 1192 Olszyna, K. J., Bailey, E. M., Simonaitis, R. and Meagher, J. F.: O_3 and NO_y relationships at a rural site,
 1193 99(D7), 14557–14563, doi:10.1029/94JD00739, 1994.
- 1194 Palmer, P. I., Abbot, D. S., Fu, T.-M., Jacob, D. J., Chance, K., Kurosu, P., Guenther, A., Wiedinmyer, C.,
 1195 Stanton, J. C., Pilling, M. J., Pressley, S. N., Lamb, B. and Sumner, A. L.: Quantifying the seasonal and
 1196 interannual variability of North American isoprene emissions using satellite observations of the formaldehyde
 1197 column, *J. Geophys. Res.*, 111, D12315, doi:10.1029/2005JD006689, 2006.
- 1198 Parrish, D. D., Allen, D. T., Bates, T. S., Estes, M., Fehsenfeld, F. C., Feingold, G., Ferrare, R., Hardesty, R.
 1199 M., Meagher, J. F., Nielsen-Gammon, J. W., Pierce, R. B., Ryerson, T. B., Seinfeld, J. H. and Williams, E. J.:
 1200 Overview of the Second Texas Air Quality Study (TexAQS II) and the Gulf of Mexico Atmospheric
 1201 Composition and Climate study (GoMACCS), *J. Geophys. Res.*, 114 (D00F13), doi: 10.1029/2009JD011842,
 1202 2009.
- 1203 Phillips, G. J., Makkonen, U., Schuster, G., Sobanski, N., Hakola, H. and Crowley, J. N.: The detection of
 1204 nocturnal N_2O_5 as HNO_3 by alkali- and aqueous-denuder techniques, *Atmos. Meas. Tech.*, 6, 231–237,
 1205 doi:10.51094/amt-6-231-2013, 2013.
- 1206 Pope, R. J., Chipperfield, M. P., Savage, N. H., Ordóñez, C., Neal, L.S., Lee, L.A., Dhomse1, S. S., Richards,
 1207 N. A. D. and Keslake, T. D.: Evaluation of a regional air quality model using satellite column NO_2 : treatment
 1208 of observation errors and model boundary conditions and emissions, *Atmos. Chem. Phys.*, 15, 5611–5626,
 1209 doi:10.5194/acp-15-5611-2015, 2015.

- 1210 Prather, M. J., Numerical advection by conservation of second-order moments, *J. Geophys. Res.*, 91, 6671–
1211 6681, 1986.
- 1212 Russell, A. R., Perring, A. E., Valin, L. C., Bucsela, E. J., Browne, E. C., Wooldridge, P. J. and Cohen, R. C.:
1213 A high spatial resolution retrieval of NO₂ column densities from OMI: method and evaluation, *Atmos. Chem.*
1214 *Phys.*, 11, 8543-8554, doi:10.5194/acp-11-8543-2011, 2011.
- 1215 Schery, S. D.: Progress on Global Rn²²² Flux Maps and Recommendations for Future Research, in: 1st
1216 International Expert Meeting on Sources and Measurements of Natural Radionuclides Applied to Climate and
1217 Air Quality Studies (Gif-sur-Yvette, France, June 2003), edited by: Barrie, L. A. and Lee, H. N., WMO TD
1218 1201, Gif-sur-Yvette, France, 43–47, 2004.
- 1219 Schwartz, S. E.: Mass-transport considerations pertinent to aqueous-phase reactions of gases in liquid-water
1220 clouds, in: *Chemistry of Multiphase Atmospheric Systems*, edited by: Jaechske, W., Springer, Heidelberg,
1221 415–471, 1986.
- 1222 Seltzer, K. M., Vizuete, W. and Henderson, B. H.: Evaluation of updated nitric acid chemistry on ozone
1223 precursors and radiative effects, *Atmos. Chem. Phys. Discuss.*, 15, 3219–3255, 2015.
- 1224 Shettle, E. P. and Fenn, R. W.: Models for the aerosols of the lower atmosphere and the effects of the humidity
1225 variations on their optical properties, *Environ. Res. Paper*, 676, AFGL-TR-79-0114, 91 pp, 1979.
- 1226 Sindelarova, K., Granier, C., Bouarar, I., Guenther, A., Tilmes, S., Stavrakou, T., Muller, J.-F., Kuhn, U.,
1227 Stefani, P. and Knorr, W.: Global dataset of biogenic VOC emissions calculated by the MEGAN model over
1228 the last 30 years, *Atmos. Phys. Chem.*, 14, 9317–9341, doi:10.5194/acp-14-9317-2014, 2014.
- 1229 Singh, H. B., Brune, W. H., Crawford, J. H., et al.: Chemistry and transport of pollution over the Gulf of
1230 Mexico and the Pacific: spring 2006 INTEX-B campaign overview and first results, *Atmos. Chem. Phys.*, 9,
1231 2301-2318, doi:10.5194/acp-9-2301-2009, 2009.
- 1232 Stavrakou, T., Müller, J.-F., De Smedt, I., Van Roozendael, M., van der Werf, G. R., Giglio, L., and Guenther,
1233 A.: Global emissions of non-methane hydrocarbons deduced from SCIAMACHY formaldehyde columns
1234 through 2003-2006, *Atms. Chem. Phys.*, 9, 3663-3679, 2009.
- 1235 Steinbacher, M., Zellweger, C., Schwarzenbach, B., Bugmann, S., Buchmann, B., Ordóñez, C., Prevot, A. S.
1236 H., and Hueglin, C.: Nitrogen oxides measurements at rural sites in Switzerland: bias of conventional
1237 measurement techniques, *J. Geophys. Res.*, 112, D11307, doi:10.1029/2006JD007971, 2007.
- 1238 Stevenson, D. S., Dentener, F. J., Schultz, M. G., Ellingsen, K., van Noije, T. P. C., Wild, O., Zeng, G.,
1239 Amann, M., Atherton, M., Bell, N., Bergmann, D. J., Bey, I., Bulter, T., Cofala, J., Collins, W. J., Derwent, R.
1240 G., Doherty, R. M., Drevet, J., Eskes, H. J., Fiore, A. M., Gauss, M., Hauglustaine, D. A., Horowitz, L. W.,
1241 Isaksen, I. S. A., Krol, M. C., Lamarque, J.-F., Lawrence, M. G., Montanaro, V., Müller, J. F., Pitari, G.,
1242 Prather, M. J., Pyle, J. A., Rast, S., Rodriguez, J. M., Sanderson, M. G., Savage, N. H., Shindell, D. T.,
1243 Strahan, S. E., Sudo, K., and Szopa, S.: Multimodel ensemble simulations of present-day and near future
1244 tropospheric ozone, *J. Geophys. Res.*, 111, D08301, doi: 10.1029/2005JD006338, 2006.

- 1245 Sutton, R. T., Dong, B. and Gregory, J. M.: Land/sea warming ratio in response to climate change: IPCC AR4
1246 model results and comparison with observations, *Geophys. Res. Letts.*, 34(2), 10.1029/2006GL028164, 2007.
- 1247 Tang, Q., Prather, M. J. and Hsu, J.: Stratosphere-troposphere exchange ozone flux related to deep convection,
1248 *Geophys. Res. Letts.*, 38, L03806, doi:10.1029/2010GL046039, 2011.
- 1249 Thouret, V., Marenco, A., Logan, J. A., Nédélec, P., and Grouhel, C.: Comparisons of ozone measurements
1250 from the MOZAIC airborne program and the ozone sounding network at eight locations, *J. Geophys. Res.*, 103,
1251 25695–25720, 1998.
- 1252 Tiedtke, M.: A comprehensive mass flux scheme for cumulus parameterization in large-scale models, *Mon.*
1253 *Weather. Rev.*, 117(8), 1779–1800, 1989.
- 1254 Tørseth, K., Aas, W., Breivik, K., Fjaeraa, A. M., Fiebig, M., Hjellbrekke, A. G., Lund-Myrhe, C., Solberg, S.
1255 and Yttri, K. E.: Introduction to the European Monitoring and Evaluation Programme (EMEP) and observed
1256 atmospheric composition change during 1972-2009, *Atmospheric Chemistry and Physics*, 12, 5447-5481,
1257 2012.
- 1258 Urban, J., Pommier, M., Murtagh, D. P., Santee, M. L. and Orsolini, Y. J.: Nitric acid in the stratosphere based
1259 on Odin observations from 2001 to 2009 – Part 1: A global climatology, *Atmos. Chem. Phys.*, 9, 7031–7044,
1260 doi:10.5194/acp-9-7031-2009, 2009.
- 1261 Valks, P., Pinardi, G., Richter, A., Lambert, J.-C., Hao, N., Loyola, D., Van Roozendaal, M., and Emmadi, S.:
1262 Operational total and tropospheric NO₂ column retrieval for GOME-2, *Atmos. Meas. Tech.*, 4, 1491-1514,
1263 doi:10.5194/amt-4-1491-2011, 2011.
- 1264 van Geffen, J.H.G.M., Boersma, K. F., Eskes, H. J., Maasakkers J. D. and Veefkind, J. P., TROPOMI
1265 Algorithm Theoretical Basis Document (ATBD) tropospheric and total NO₂, S5P-KNMI-L2-0005-RP, 56pp,
1266 2016.
- 1267 van der A, R. J., Allaart, M. A. F., and Eskes, H. J.: Multi sensor reanalysis of total ozone, *Atmos. Chem. Phys.*
1268 *Discuss.*, 10, 11401-11448, doi: 10.5194/acpd-10-11401-2010, 2010.
- 1269 van der Werf, G. R., Randerson, J. T., Giglio, L., Collatz, G. J., Mu, M., Kasibhatla, P. S., Morton, D. C.,
1270 DeFries, R. S., Jin, Y., and van Leeuwen, T. T.: Global fire emissions and the contribution of deforestation,
1271 savanna, forest, agriculture, and peat fires (1997–2009) *Atmos. Chem. Phys.*, 10, 11707–11735, 2010,
1272 <http://www.atmos-chem-phys.net/10/11707/2010/>.
- 1273 Veefkind, J.P., Aben, I., McMullan, K., Förster, H., de Vries, J., Otter, G., Claas, J., Eskes, H. J., de Haan, J.
1274 F., Kleipool, Q., van Weele, M., Hasekamp, O., Hoogeveen, R., Landgraf, J., Snel, R., Tol, P., Ingmann, P.,
1275 Voors, R., Kruizinga, B., Vink, R., Visser, H. and Levelt, P. F.: TROPOMI on the ESA Sentinel-5 Precursor:
1276 A GMES mission for global observations of the atmospheric composition for climate, air quality and ozone
1277 layer applications, *Remote. Sens. Environ.*, 120, 70-83, doi:10.1016/j.rse.2011.09.027, 2012.
- 1278 Verstraeten, W. V., Neu, J. L., Williams, J. E., Bowman, K. W. and Worden, J. R.: Rapid increases in
1279 tropospheric ozone production and export from China, *Nature Geosci.*, 8, 690-695, doi: 10.1038/ngeo2493,
1280 2015.

- 1281 Vinken, G. C. M., Boersma, K. F., Jacob, D.J. and Meijer, E. W.: Accounting for non-linear chemistry of ship
 1282 plumes in the GEOS-Chem global chemistry transport model, *Atms. Chem. Phys.*, 11, *Atmos. Chem. Phys.*,
 1283 11707-11722, doi:10.5194/acp-11-11707-2011, 2011.
- 1284 Vinken, G. C. M., Boersma, K. F., Maasakkers, J. D., Adon, M. and Martin, R. V.: Worldwide biogenic soil
 1285 NO_x emissions inferred from OMI NO₂ observations, *Atmos. Chem. Phys.*, 14, doi:10.5194/acp-14-10363-
 1286 2014, 10363–10381, 2014.
- 1287 Vogelesang, D. H. P. and Holtslag, A. A. M.: Evaluation and model impacts of alternative boundary-layer
 1288 height formulations, *Bound.-Layer Meteor.*, 81, 245–269, 1996.
- 1289 Von Kuhlmann, R. and Lawrence, M. G.: The impact of ice uptake of nitric acid on atmospheric chemistry,
 1290 *Atms. Chem. Phys.*, 6, 225-235, 2006.
- 1291 Wild, O. and Prather, M. J.: Global tropospheric ozone modeling: Quantifying errors due to grid resolution, *J.*
 1292 *Geophys. Res.*, 111, D11305, doi:10.1029/2005JD006605, 2006.
- 1293 Williams, J. E., Strunk, A., Huijnen, V. and van Weele, M.: The application of the Modified Band Approach
 1294 for the calculation of on-line photodissociation rate constants in TM5: implications for oxidative capacity,
 1295 *Geosci. Model Dev.*, 5, 15-35, doi:10.5194/gmd-5-15-2012, 2012.
- 1296 Williams, J. E., van Velthoven, P. F. J., and Brenninkmeijer, C. A. M.: Quantifying the uncertainty in
 1297 simulating global tropospheric composition due to the variability in global emission estimates of Biogenic
 1298 Volatile Organic Compounds, *Atmos. Chem. Phys.*, 13, 2857–2891, doi: 10.5194/acp-13-2857-2013, 2013.
- 1299 Williams, J. E., Le Bras, G., Kukai, A., Ziereis, H., and Brenninkmeijer, C. A. M.: The impact of the chemical
 1300 production of methyl nitrate from the NO + CH₃O₂ reaction on the global distribution of alkyl nitrates, nitrogen
 1301 oxides and tropospheric ozone: a global modeling study, *Atmos. Chem. Phys.*, 14, 2363-2382, 2014.
- 1302 Worden, J., Liu, X., Bowman, K., Chance, K., Beer, R., Eldering, A., Gunson, M. and Worden, H., Improved
 1303 tropospheric ozone profile retrievals using OMI and TES radiances, *Geophys. Res. Lett.*, 34, L01809,
 1304 doi:10.1029/2006GL027806, 2007.
- 1305 Yamaji, K., Ikeda, K., Irie, H., Kurokawa, J. and Ohara, T.: Influence of model grid resolution on NO₂ vertical
 1306 column densities over East Asia, *J. Air. Waste Manage. Assoc.*, 64(4), 436-444, 2014.
- 1307 Yarwood, G., Rao, S., Yocke, M., and Whitten, G.: Updates to the carbon bond chemical mechanism: CB05,
 1308 Final report to the US EPA, EPA Report Number: RT-0400675, available at: www.camx.com (last access: 15
 1309 January 2014), 2005.
- 1310 Zhang, K., Feichter, J., Kazil, J., Wan, H., Zhuo, W., Griffiths, A. D., Sartorius, H., Zahorowski, W., Ramonet,
 1311 M., Schmidt, M., Yver, C., Neubert, R. E. M. and E.-G. Brunke, E.-G.: Radon activity in the lower troposphere
 1312 and its impact on ionization rate: a global estimate using different radon emissions, *Atmos. Chem. Phys.*, 11,
 1313 7817–7838, doi:10.5194/acp-11-7817-2011, 2011.
- 1314 Zeng, G., Williams, J. E., Fisher, J.A., Emmons, L. K., Jones, N. B., Morgenstern, O., Robinson, J., Smale, D.,
 1315 Paton-Walsh, C. and Griffith, D. W. T.: Multi-model simulation of CO and HCHO in the Southern

- 1316 Hemisphere: comparison with observations and impact of biogenic emissions, *Atmos. Chem. Phys.*, 15, 7217-
1317 7245, doi:10.5194/acp-15-7217-2015, 2015.
- 1318 Zdunkowski, W. G., Welsch, R. M., and Kord, G. J.: An investigation of the structure of typical 2-stream
1319 methods for the calculation of solar fluxes and heating rates in clouds, *Contrib. Atmos. Phys.*, 53, 215-238,
1320 1980.
- 1321 Zhou, Y., Brunner, D., Hueglin, C., Henne, S., and Staehelin, J.: Changes in OMI tropospheric NO₂ columns
1322 over Europe from 2004 to 2009 and the influence of meteorological variability. *Atmos Environ*, 46, 482-495,
1323 2012.
- 1324 Zyrichidou, I., Koukouli, M. E., Balis, D., Markakis, K., Poupkou, A., Katragkou, E., Kioutsioukis, I., Melas,
1325 D., Boersma, K. F. and van Roozendaal, M.: Identification of surface NO_x emission sources on a regional
1326 scale using OMI NO₂, *Atms. Environ.*, 101, 82-93, 2015.